POLITECNICO
MILANO 1863

Methane for regenerative cooling purposes

A numerical and experimental investigation of cooling performances and related phenomena

MSc thesis in Space Engineering

Author: **Francesco Ceglie**

Student ID: 247289
Supervisors: prof. Christian Paravan, prof. Jens Fridh
Co-supervisor: Jules Heldens
Academic Year: 2024-25

Abstract (in lingua italiana)

Di recente, l'impiego del metano come combustibile sta suscitando un crescente interesse nel settore spaziale grazie all'elevata efficienza in termini di prestazioni di spinta, alla favorevole densità di stoccaggio e alle prospettive strategiche offerte dall'utilizzo di risorse in situ. Inoltre, esso si presta particolarmente alla riutilizzabilità dei lanciatori, caratteristica che sta trovando sempre più spazio tra i sistemi di lancio. Tuttavia, la decomposizione termica del combustibile nei sistemi di raffreddamento rigenerativo può compromettere l'integrità degli stessi. Parallelamente, le tecnologie di manifattura additiva stanno trovando un crescente utilizzo per la realizzazione di componenti per propulsori aeronautici e spaziali. Le prestazioni di raffreddamento dei canali rigenerativi risultano fortemente influenzate sia dalle proprietà del fluido refrigerante sia dalla rugosità dei canali. Il seguente studio si presta ad analizzare tali proprietà di raffreddamento in un canale rugoso realizzato in lega Haynes 230 mediante additive manufacturing, nonché gli effetti del cracking termico sui successivi riutilizzi dello stesso apparato. Prove sperimentali e analisi numeriche sono state condotte nell'ambito del progetto MERiT, inaugurato nel 2017 come collaborazione tra KTH e GKN Aerospace e finanziato da Swedish Space Agency, ESA (FLPP) e GKN, volto ad analizzare il metano come fluido refrigerante in sistemi di raffreddamento rigenerativo ad impiego spaziale. Le simulazioni numeriche sono state finalizzate alla valutazione dell'accuratezza di un modello industriale per la stima della correzione termica in presenza di superfici rugose. Inoltre, è stata condotta una campagna sperimentale per valutare l'effetto della formazione di coke sul degrado dell'assorbimento di calore, confrontando i coefficienti di scambio termico determinati sperimentalmente in condizioni operative comparabili prima e dopo un test ad alta temperatura. Considerate le incertezze associate alle condizioni sperimentali e alla modellizzazione, le simulazioni numeriche hanno evidenziato un'accuratezza ritenuta soddisfacente. Il confronto tra i casi con eventuale deposizione carboniosa e non, ha presentatato possibili tracce di un eventuale degradazione termica. Tuttavia, tali riscontri dovranno essere ulteriormente contestualizzati mediante successive analisi.

Keywords: metano; raffreddamento rigenerativo; rugosità; cracking termico

Abstract

Methane as a fuel has been drawing increasing interest in the space sector owing to its efficiency in terms of offered thrust performances compared to storing capabilities and strategic in-situ resource utilisation. Additionally, it lends itself to reusable system, whose development experienced a remarkable surge in the most recent years. However, fuel thermal decomposition in regenerative cooling systems may compromise such a characteristic and its related advantages. At the same time, additive manufacturing techniques for engine components realisation are progressively taking hold in the field. Regenerative cooling jackets cooling performances are strongly affected both by the coolant and channel surface roughness. The present study aims to investigate methane cooling performances through a Haynes230 additive manufactured rough channel as well as thermal cracking phenomenon effects on subsequent uses of the same apparatus. Experimental trials and numerical analysis have been conducted within MERiT framework, a research project focusing on methane characterisation for regenerative cooling in rocket nozzles, started in 2017 as a collaboration between KTH and GKN Aerospace and funded by the Swedish Space Agency, ESA (FLPP) and GKN. In the present work, the assessment of prediction accuracy of an industrial thermal correction model in numerically recreating the channel thermal field at different fluid flow conditions has been performed. Additionally, a suited test campaign has been conducted to seize the effect of coking on heat transfer degradation in the test article, by comparing the experimentally retrieved heat transfer coefficients for similar test conditions previous and after a high temperature trial. The numerical prediction revealed sufficiently accurate for the lowest analysed mass flow rates. On the other hand, highest Reynolds number test points revealed to be affected by an higher uncertainty both related to the experimental conditions and the numerical modelling. The comparison between the coked and clean cases generally revealed an heat transfer degradation, possibly related to a coking layer formation. Nonetheless, these outcomes should be contextualised though further analysis.

Keywords: methane; regenerative cooling; roughness; thermal cracking

AI declaration statement

ChatGPT (OpenAI, GPT-5.2, 2026) was employed for language editing purposes, including lexical and grammatical refinement of the present document. The author declares that all the contents developed in this work fall entirely under the intellectual responsibility and intellectual property of the author.

Contents

A suor Maria Luisa, mia prima maestra di vita.

1 | Introduction

Since Sputnik 1, the first space object ever to be placed into orbit in 1957, access to space has been progressively eased. Launchers have evolved through the decades to suit the needs and ambitions of the space sector, from the deployment of small scale satellites to the delivery of crewed modules. Recently, reusability has drawn increasing interest as this characteristic allows to "recycle" part of the launch systes, especially the first stages, reducing operational costs, provided that a minimum number of reuse cycles is achieved. Nowadays such a feature is being widely investigated at propulsion system level, focusing on phenomena that could compromise the engine integrity over subsequent operations. Among the equipment, hydrocarbon-based regenerative cooling systems are particularly sensitive to degradation due to thermal decomposition of fuel compounds. Indeed, the high temperatures experienced can lead to significant carbon layers deposition on channel inner walls, ultimately affecting the cooling performance over time and repeated usages. At the same time, methane has recently emerged as one of the most promising propellant for several technical and strategic reasons. A higher specific impulse compared with RP-1 leads to enhanced engine performance, while its increased density and higher storage temperature compared to cryogenic hydrogen enable a definitely lighter and simpler storage and feed system. Furthermore, methane can be produced directly from Sabatier cycle, which requires water and carbon dioxide as inputs, elements that are readily accessible on Mars surface for in-situ resource utilization (ISRU), a feature that makes this fuel doubly appealing in terms of refuelling operations.

On the other hand, recent advances in additive manufacturing (AM) technologies have significantly expanded the design capabilities of regenerative cooling systems, enabling the realization of complex internal channel geometries with a high degree of geometric flexibility. As a result, AM processes are increasingly being adopted in the aerospace sector for the production of both entire engine sub-assemblies and components, such as combustion chambers, injector heads, and thrust chamber liners, where integrated cooling architectures are required. Techniques such as laser powder bed fusion (LPBF) allow for the fabrication of cooling passages tailored to local thermal loads and stringent geometric constraints. However, these manufacturing advantages are inherently associated

with internal surfaces characterized by relatively rough internal surfaces, originating from partially melted powder particles, layer-wise fabrication, and process-induced defects. Experimental and numerical investigations reported in the literature demonstrated that AM-induced roughness is strongly dependent on process parameters, build orientation, and post-treatment approaches. From a thermofluid perspective, wall roughness has a pronounced impact on coolant flow behaviour, conditioning boundary layer development, turbulence intensity, heat transfer, and pressure losses. Consequently, the thermal performance of additively manufactured regenerative cooling systems is closely linked to the interaction between rough elements and flow dynamics, making the accurate characterization of AM-induced roughness a key aspect in the design and evaluation of high-efficiency cooling architectures.
Because of the considerable and recent surge of interest in methane as a propellant for reusable engines, researches addressing methane cooling performances in regenerative apparatuses are progressively bridging the gap between its application in existing systems (such as under development engines like Raptor and BE-4) and a comprehensive understanding of its use in space propulsion. Alongside investigations into fuel characteristics, AM techniques are gaining increasing attention in the field and are progressively reshaping the landscape of engines components manufacturing.

The present work aims to further enlarge our comprehension about this fuel in regenerative apparatuses for space applications, encompassing both its heat absorption performances and coking effects on heat transfer, especially when coupled with channels additively manufacturing features. Although the aspects addressed in the following discussion do not converge toward a detailed assessment of reusability, the author wishes that the present dissertation can offer useful insights for specialised future inquiries. In particular, this study consists of both numerical and experimental analysis of methane characteristics and related phenomena in regenerative cooling AM channel. The experimental advancements presented in this work are credited to the MERiT project, developed by EGI department at Kungliga Tekniska högskolan (KTH), in collaboration with GKN Aerospace, and funded by the Swedish National Space Agency, as well as all its participants who the author express his gratitude to. The following introductory sections will provide the reader with further information into the subject of analysis together with a detailed depiction of the operative framework just mentioned.

1.1 Experimental facility potential for methane characterisation and previous related works

MERiT experimental set-up presents suitable features for the investigation of methane cooling performances in the exit regions of regenerative systems closer to the injection plate, where the fluid has already reached supercritical state after absorbing part of the heat from the hot gases flowing through the combustion chamber. At the rear end of these systems the coolant can reach significant temperature levels, potentially exceeding the decomposition onset temperature of hydrocarbon-based fuel. The project has been coherently conceived with the aim of analysing methane thermal cracking and its effect on cooling performances. Its development and implementation have been coordinated by EGI Department at KTH University in collaboration with GKN Aerospace, which remain a key partner in providing experienced guidance, support and test configurations.
In a nutshell, the experimental measurement system encompasses a series of sensors that probe fluid properties and test rig temperatures at prescribed locations to partly reconstruct the thermal field established under adjustable flow and heating conditions. A test channel is lodged into a one-side heated copper block equipped with electrical cartridges capable of providing a power of 400 W each. Moreover, the gas can be preheated upstream the test section up to a temperature of 655 K, while the mass flow rate and back pressure can be regulated accordingly to the available feed pressure, thereby recreating typical operating conditions experienced in regenerative cooling systems. The test article consists of a single cooling channel whose geometry is completely comparable with the cavities typically employed in combustion chambers jackets. Measurements can be used to trace back to the Heat Transfer Coefficient (HTC) at different longitudinal stations by reconstructing the established flow field from probed boundary conditions.

Several works have been conducted previously within the MERiT project. Ristic [1] approached the test rig design and developed an initial numerical model for its preliminary analysis, probing different concepts to maximize the heat pick-up and highlighting the rig capabilities and limitations. This model was further refined by Pettersson [2], who focused his analysis on exploring multiple potential test points and the corresponding rig behaviour for different test article configurations and materials. Recently, Heldens et al. [3] carried out an experimental investigation of methane cooling performances using one of the previously analysed configurations, developing a suited methodology for data processing based on the available experimental instrumentation.
The present dissertation builds on the wake of the aforementioned works and aims to advance both the numerical and experimental frameworks developed so far. Specifically,

as additively manufactured configurations became part of the MERiT program interests, additional modelling factors became relevant for producing an accurate numerical representation of test conditions. The last updated CFD model developed by Petterson, in fact, did not considered the effect of surface roughness in the analysed channels with respect to both pressure drop and heat transfer, which reveals to significantly affect simulation outputs. Furthermore, the methodology employed by Heldens et al. [3] required compromises related to the available set of sensors in the test rig. For example, a constant heat flux toward the inner walls of the channel was assumed to compute the inner surface temperatures from the available outputs located at the channel baseline, and a linear trend of pressure and temperature was assumed in the fluid flow to retrieve bulk values at the corresponding sensors stations. These assumptions were suitable for the purposes of the previous study, but could lead to data misinterpretation, especially in this phase of the project where numerical and empirical results need to be compared to compensate for the limited measurement capability within the flow.

1.2 Thesis objectives and Workflow overview

Having a clearer view of the challenges related to the topic and of the resources available at the EGI Department, the objectives of this study have been defined and are presented in Table 1.1.

Research objectives
To experimentally investigate the heat transfer performances of methane for a defined channel configuration while refining the existing model for experimental data processing.
To adapt the existing numerical model to the present experimental configuration by accounting for channel internal roughness and assess its reliability through a direct comparison with the obtained empirical data.
To explore new approaches for the assessment of methane thermal decomposition, especially in terms of heat transfer degradation affecting the system over subsequent uses.

Table 1.1: Objectives of analysis

In light of the presented objectives, the present work focuses on a combined numerical and experimental investigation of methane cooling performance in a single AM channel realized with Haynes230 alloy. The channel test section has been modelled with CAD software and

meshed in accordance with previous implemented numerical model and used to conduct simulations with this specific channel configuration employed during trials. Numerical simulations have been performed with Ansys® CFX to reproduce flow conditions analysed during experimental campaigns, thus providing deeper insight into the channel-established thermal field. At the same time, the model has been refined with respect to past numerical assessments by considering the effect of internal surface roughness, which may significantly influence the heat transfer.

The present analysis will also offer additional insight into system performance when thermal decomposition of methane occurred, with the aim of quantifying the effects of carbon layer deposition on the channel inner surfaces in terms of heat transfer coefficient deterioration. To this end, a dedicated experimental campaign consisting of three specific trials has been conducted. Chronologically, a first trial has been performed with low input heat input supplied to the channel to avoid thermal cracking and to provide an unambiguous view of the system performance under nominal conditions. The second run aims for the channel cocking, thereby requiring higher input power and longer test duration for methane to reach the decomposition temperature and for carbon to substantially accumulate onto the inner surface so that a quantifiable heat transfer deterioration can be appreciated. The third trial is intended to reproduce the operating conditions of the first while preventing additional carbon deposition, thereby enabling a meaningful comparison between the coked and clean cases.

To facilitate the reader's orientation, the present document is structured as follows. Chapter 2 introduces the theoretical background and reviews the experimental concepts underlying regenerative cooling system assessment, thereby establishing the foundation of this work. Chapter 3 provides a detailed description of the MERiT experimental facility, including its equipment and instrumentation as well as test article characteristics. Chapter 4 presents the adopted methodology, addressing both the experimental and numerical models together with their underlying assumptions and limitations. Chapter 5 discusses the research outcomes and their interpretation. Chapter 6 summarizes the main findings, while Chapter 7 outlines potential future developments in light of the results obtained.

2 | Theoretical background and Literature review

The present chapter provides the theoretical framework and literature background which this study builds upon. The fundamental mechanisms governing heat transfer and fluid flow in rough cavities are first introduced with particular insights in surface roughness characterization, rough-wall turbulence and their influence on friction and heat transfer. The discussion then addresses methane as a coolant, focusing on its thermophysical behaviour, thermal decomposition processes, and catalytic interactions with metallic materials. Finally, existing experimental methodologies and data-reduction techniques are reviewed to contextualize the MERiT facility approach.

2.1 Roughness characterisation

The intrinsic stochastic nature of surface roughness poses great challenges in their representation for physical analysis purposes. Rough surfaces are usually described through statistical descriptors which can properly capture their irregular distributions. To this end, international standards such as ASME Y14.36M and ISO 1302 define a comprehensive set of parameters for surface roughness characterization [4]. These can be evaluated either along a sampling line, yielding R-type values, or over a sampling area, referred to as S-type parameters, which generally provide a more representative description of complex surface morphologies . Table 2.1 gathers some of the widely adopted metrics for surface roughness characterisation [4] according to the reference frame shown in Figure 2.1.

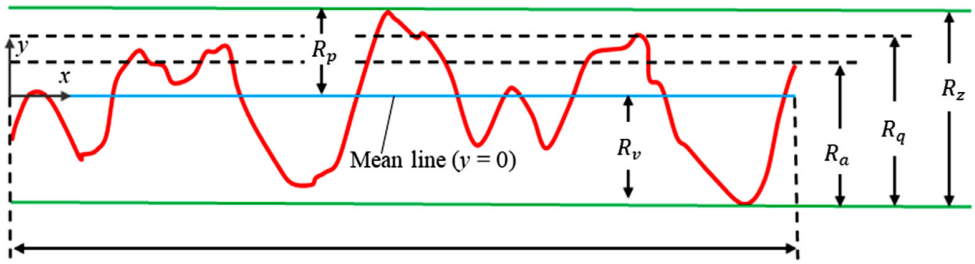

Figure 2.1: Qualitative representation of roughness metrics. Image from Kadivar et al. [4].

Parameter	Description	Mathematical description
R_a	Arithmetic mean deviation	$\frac{1}{l}\int_0^l \lvert y(x)\rvert\, dx$
R_q	Root-mean-square roughness	$\sqrt{\frac{1}{l}\int_0^l y^2(x)\, dx}$
R_v	Maximum valley depth below the mean line	$\lvert\min y(x)\rvert$
R_p	Maximum peak height above the mean line	$\max y(x)$
R_z	Maximum peak-to-valley height of the profile	$R_v + R_p$
s_k	Skewness	$\frac{1}{R_q^3}\frac{1}{l}\int_0^l y^3(x)\, dx$
k_u	Kurtosis	$\frac{1}{R_q^4}\frac{1}{l}\int_0^l y^4(x)\, dx$

Table 2.1: Definition of roughness parameters.

Among these metrics, amplitude parameters quantify the vertical deviations of surface profile from the mean plane, corresponding to the xz plane in Figure 2.1, based on height-map data. The arithmetic mean roughness R_a is broadly used but it often lacks physical significance if not coupled with any other descriptors. Distinct surface morphologies, in fact, may exhibit identical R_a values. Conversely, the root mean square roughness R_q, corresponding to the standard deviation of the surface height distribution, provides a more robust statistical interpretation. The R_z parameter further enhances sensitivity to extreme features, effectively capturing isolated high peaks or deep valleys. Skewness indicates the asymmetry of the height distribution and reflects the predominance of peaks or valleys. For example, symmetric and Gaussian-like morphologies exhibit zero skewness, whereas deposition-dominated or eroded surfaces result in positive or negative skewness, respectively. Kurtosis quantifies the sharpness of the height distribution, distinguishing between flattened profiles ($k_u < 3$) and surfaces dominated by sharp asperities and deep

troughs ($k_u > 3$) [4].

Considering the multiple features of surface roughness topography described through the aforementioned indicators, it becomes evident how flow characteristics over rough surfaces could be directly related to a consistently wide set of parameters. For engineering analysis, it is convenient to enclose such properties effects on the mean flow field into a single length scale capable of characterising roughness elements. To this end, the equivalent sand-grain roughness approach, stemming from Nikuradse [5] and Schlichting [6] groundbreaking works, has been widely adopted by the scientific community ever since. As clearly explained by Kadivar et al. [4], take as reference a surface covered with a single layer of uniformly packed spheres as illustrated in Figure 2.2a. Such spheres diameter is defined as *sand-grain roughness height* k. Whenever the roughness elements morphology consistently differs from a spherical shape, as is the case for most industrial roughness types, the sand-grain roughness cannot be readily derived as such. As shown in Figure 2.2b, Colebrook and White [7] then introduced the *equivalent sand-grain roughness* k_s as an analogous height for irregular surface, such that the friction experienced on this type of surface in the so-defined fully rough regime matches that observed for a sand-grained surface with $k = k_s$. The definition of the fully rough regime is presented in the following sections.

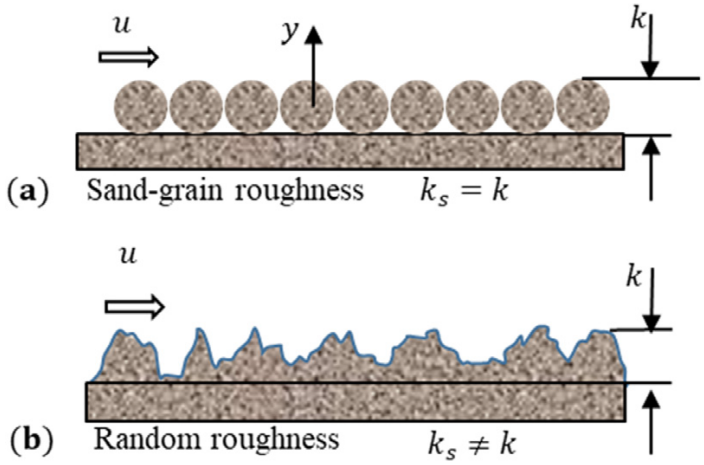

Figure 2.2: Equivalent sand-grain roughness. Image from Kadivar et al. [4].

It is worth mentioning that several attempts have been made to correlate the equivalent sand-grain roughness with conventional surface metrics or roughness statistical distribution descriptors, through both numerical and experimental approaches. Kadivar et al. [4] provides a comprehensive overview of these correlations, whose applicability is generally limited to restricted types of roughness. Among these studies, Stimpson et al. [8] investigated surface roughness in direct metal laser sintered (DMLS) minichannels to establish

a quantitative link between physical roughness metrics and flow behaviour. Owing to a comparison with experimental flow data, the analysis revealed a prominent dependence between the arithmetic mean roughness to hydraulic diameter ratio, Ra/D_h, and the equivalent sand grain roughness to hydraulic diameter ratio, k_s/D_h. This result appears to contrast with the limited physical significance of the arithmetic mean height alone, as well with most empirical correlations, which oppositely refer to more representative roughness metrics. Nonetheless, as remarked by Kadivar et al. [4], the constrained nature of channel flows, which limits the boundary layer development, has a undeniable influence on flow characteristics. This aspect conditions roughness effects on flow behaviour compared with external flows, which were taken as reference for most of those correlations that did not suited Stimpson's findings. This topic will be addressed in detail in Section 2.2.

2.2 Flows in rough channels

Heat transfer in fluid flows is strongly related to both the flow regime and the features of the boundary layer region near a wall surface. When the analysis is restricted to turbulent smooth-wall pipe flows, two distinct regions can be identified: a turbulent core, characterized by strong velocity fluctuations and intrinsic stochastic behaviour, and a boundary layer developing between the core flow and the surface, where velocity profile develops from the no-slip condition at the wall. As reviewed by Kadivar et al. [4], this turbulent boundary layer can be further divided into an "inner" and "outer" region. The inner one, closest to the surface, is actively influenced by fluid viscosity and local flow parameters, whereas the outer region, shaped by the neighbouring core turbulent stresses, is relatively insensitive to the underlying zone as well as to surface geometry [9]. The inner region itself can be further subdivided into three well-known layers that, moving from the wall toward the outer boundary layer, are the viscous sublayer, the buffer layer and the logarithmic layer. Figure 2.3 illustrates their extension in terms of dimensionless wall distance y^+, together with the typical dimensionless wall velocity U^+ profile observed in both experimental investigations and modelled through widely accepted formulations. The viscous sublayer and the logarithmic layer are mainly dominated by viscous and turbulent Reynolds stresses, respectively. The buffer layer bridges these two zones, featuring comparable levels of stress intensity ascribable to both fluid viscosity and turbulence-induced viscosity. At the same time, high velocity gradients occur in this region, making it the main contributor to turbulence generation within the boundary layer.

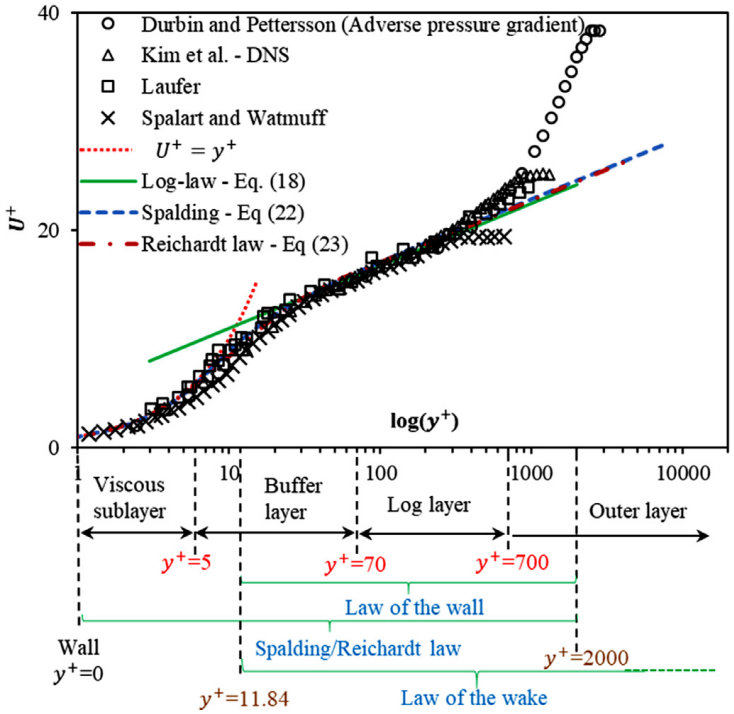

Figure 2.3: Mean velocity profile for zero and adverse pressure gradient boundary layer flow compared to experimental data. Image from Kadivar et al. [4].

With these preliminary notions in mind, at this stage of the dissertation it is possible to introduce those concepts and theories necessary to account for surface roughness in turbulent flows analysis and its impact on the resulting fluid field. Again, Kadivar et al. [4] highlighted how current engineering models for surface roughness treatment are largely based on extensions of turbulent flows over smooth wall, accounting for the "small" perturbations induced by roughness elements. To clarify this approach, it is of paramount importance recalling the Reynolds number similarity hypothesis, which states that flows occurring in geometrically similar structures are dynamically similar when their Reynolds numbers are equal. Moreover, Townsend [10] underlined another key aspect, noting that fully established turbulent flow fields[1] in similar geometrical structures are also closely similar. Building on this reasoning, Townsend formulated what was later labelled as the *wall similarity hypothesis* for turbulent flow over smooth and rough walls, which can be expressed as follows:

> "The existence of the viscous layer shows that the whole flow cannot be independent of the fluid viscosity, and the principle of Reynolds number similarity can be applied only to the fully turbulent region in which the direct effects of

[1]This means that the Reynolds number for that specific flow is large enough to be considered completely turbulent.

> the viscous stresses are negligible. If the viscous layers are thin compared to the channel width, the defining parameter for the fully turbulent region are the channel width and the velocity conditions and the stresses at the boundary of the region" Townsend [10, p. 133]

In summary, according to Townsend's theory, for sufficiently high Reynolds numbers the turbulent motions outside the viscous sublayer are independent of the surface profile and fluid viscosity. Consequently, other flow parameters being equal, the core flow conditions in rough and smooth channels can be considered comparable. Nevertheless, it must be remarked that such an hypothesis does not completely isolate the influence of surface roughness on the core flow field behaviour. Indeed, what clearly differs between the the two cases is undoubtedly the wall shear stresses associated with the near-wall region, which directly influence the friction factor and pressure drop within the channel. Roughness elements, in fact, transmit additional shear stresses to the wall due to the pressure differences developing between upstream and downstream facing surfaces. Moreover, it can be further deduced that in the near-wall region flow characteristics are determined exclusively on local conditions such as wall distance, wall shear stresses, fluid viscosity and surface profile [11].
The wall similarity hypothesis has found support in several experimental studies and has been validated through suitable direct numerical simulations (DNS) that Kadivar et al. [4] accurately described. On the other hand, exceptions have also been observed. Such anomalies concern channel configurations in which roughness elements protrude into the inner layer thickness, disrupting a significant portion of the logarithmic region. Flack et al. [12] reported disparate behaviours for flows over surface with "strong" roughness. In light of their findings, such flows were classified according to the criterion reported in Eq. (2.1).

$$\delta/k_s < 40 \tag{2.1}$$

Where δ is the boundary layer thickness and k_s the equivalent sand-grain roughness. This finding has far-reaching implications for channel flows in which the boundary layer thickness is constrained by the cross-section dimensions, especially in mini and microchannels. According to the classification proposed by Kandlikar [13], such structures exhibit a minimum characteristic cross-section dimension between 3 mm and 200 μm for minichannels, and from 200 μm to 10 μm for microchannels. With reference to the present analysis, regenerative cooling systems for space applications often employ minichannel configurations. Therefore, wall similarity hypothesis-based formulations and predictions may result

misleading for regenerative channels with particularly narrow geometries.

While defining the equivalent sand-grain roughness in Section 2.1, the fully turbulent regime has been introduced as a reference condition to relate general type roughness types to the equivalent sand-grain roughness by comparing the effect of surface asperities on flow features. Surface roughness modifies the conventional law-of-the-wall by reshaping the near-wall flow structure. Within this context, the roughness Reynolds number presented in Eq. (2.2) is introduced.

$$k_s^+ = \frac{k_s U^*}{\nu} \tag{2.2}$$

where k_s is the equivalent sand-grain roughness height, U^* is the friction velocity, and ν is the kinematic viscosity. The value of k_s^+ plays a fundamental role in classifying turbulent wall-bounded flows into distinct regimes. Three main flow conditions are distinguished and described hereafter:

- **Hydraulically smooth regime**: for $k_s^+ < k_{\text{Smooth}}^+$, the roughness elements are entirely contained within the viscous sublayer and do not affect the skin-friction coefficient or overall drag.
- **Transitionally rough regime**: for $k_{\text{Smooth}}^+ < k_s^+ < k_{\text{Rough}}^+$, both viscous and pressure forces contribute to the skin friction. In this regime, drag depends on both the Reynolds number and the relative roughness, due to the reduction of the viscous sublayer thickness and the weakening of wall-damping effects.
- **Fully rough regime**: for $k_s^+ > k_{\text{Rough}}^+$, roughness elements protrude into the fully turbulent region. As a consequence, the viscous sublayer is completely destroyed and the logarithmic velocity profile is shifted downward. The resulting friction drag is dominated by pressure forces and becomes independent of fluid viscosity and Reynolds number.

The threshold parameters k_{Smooth}^+ and k_{Rough}^+, corresponding to the onset of the transitionally rough and fully rough regimes respectively, vary across different roughness morphologies. Some of these values are available in the review by Kadivar et al. [4]. For sand-grain roughness type, for example, such boundary values are $k_{\text{Smooth}}^+ = 2.5$ and $k_{\text{Rough}}^+ = 90$, according to the findings by Cebeci [9]. Such variability reflects the difficulty of defining universal scaling parameters and has been linked to differences in the shape of the roughness function, which may exhibit monotonic behaviour or inflection points.

The flow region directly influenced by surface roughness is termed as roughness sublayer,

located beneath the logarithmic layer and representing the rough-wall analogue of the viscous sublayer. Throughout this area, turbulence levels are markedly elevated due to interactions with roughness elements. A qualitative illustration of the roughness-modified wall velocity field is presented in Figure 2.4. Roughness sublayer extension is usually estimated as $2h \leq y \leq 5h$, where h is the roughness height measured from the wall according to the definition by Raupach et al. [14]. A more universal description based on the equivalent sand-grain roughness suggests, instead, an extent of $3k_s \leq y \leq 5k_s$, providing a consistent measure of the influence of surface roughness on the mean velocity field [4].

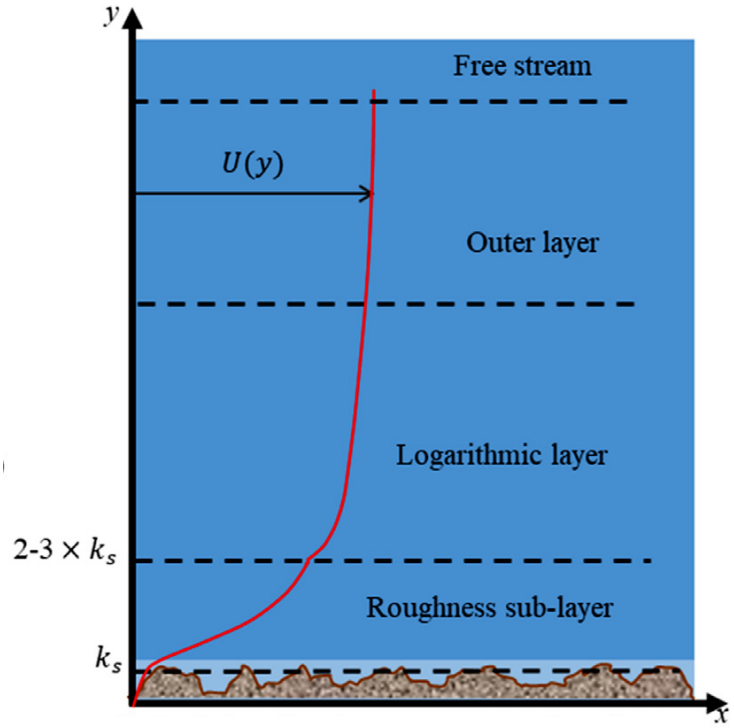

Figure 2.4: Turbulent flow layers over rough surface. Image from Kadivar et al. [4].

Having qualitatively depicted the flow characteristics over rough surfaces, it is necessary for the purposes of the present dissertation to introduce the engineering models available to quantitively capture roughness influence on flow variables. At present, such approaches are largely based on extensions of smooth surfaces characteristics to rough surfaces, which, in turn, reshape the velocity field and temperature profile. As previously mentioned, asperities alter the turbulent boundary layer by intensifying near-wall momentum exchange, thereby increasing wall shear stresses and, as a direct consequence, enhancing heat and mass transfer. As the roughness effect strengthens, the viscous sublayer is progressively weakened and may be partially disrupted in transitionally rough regimes or completely

suppressed under fully rough conditions. Despite these strong local disturbances, the wall similarity hypothesis suggests that roughness-induced perturbations remain confined to the inner region of the boundary layer, leaving the outer flow largely unchanged. As noted earlier, these alterations with respect to smooth cases are mainly concentrated within the so-called roughness sublayer. Consistent with this observation, comparisons of mean velocity profiles show that rough surfaces preserve inner-layer similarity while experiencing a systematic downward shift relative to smooth walls. This trend is evident in Figure 2.5, which compares the inner-layer mean velocity profile for zero pressure gradient turbulent boundary layers. The reshaping effect attributable to roughness presence translates into a mere downward displacement referred to as ΔU^+ [4].

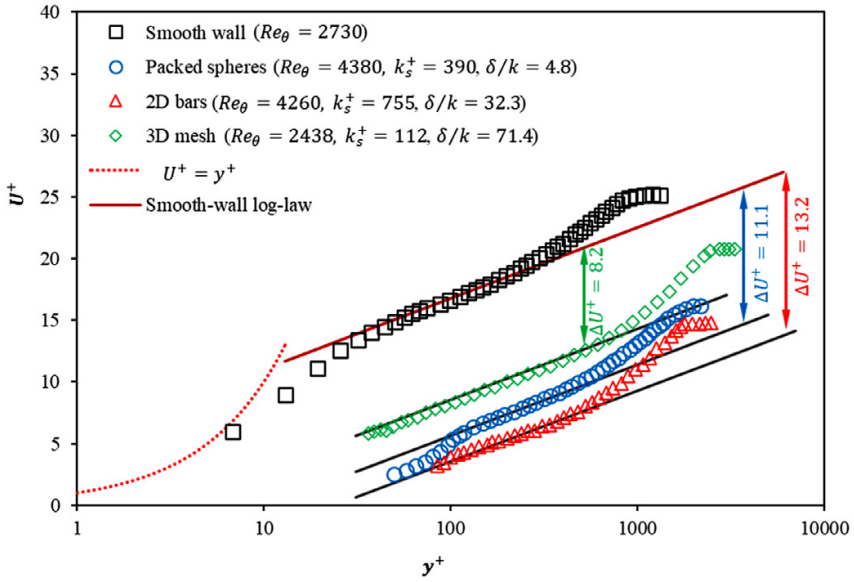

Figure 2.5: Mean velocity profile comparison between smooth and different rough surfaces with experimental data available in literature. Image from Kadivar et al. [4].

Given the above considerations, one may wonder how to quantify this velocity shift for practical engineering analysis. As reviewed by Östlund [15], within the equivalent sand-grain roughness framework two main methods can be employed to account for the velocity shift effect in numerical simulations. The first approach consists of applying a mean velocity correction directly to the smooth wall log-law. The shift factor can be obtained through appropriate roughness functions that correlate the velocity displacement with the roughness Reynolds number as $\Delta U^+ = f(k_s^+)$ and other constants related to the specific roughness type. A wide variety of such functions available in the literature underlines a key observation drawn by Flack and Schultz [16]: since no "universal" roughness function exists, no single roughness length scale can characterize all roughness types in all

roughness regimes [4]. Therefore, the presented methodology for roughness treatment would require a more detailed analysis that is beyond the scope of this dissertation. The second strategy, developed by Aupoix and Spalart [17] within the Spallart-Allarmas (SA) turbulence model, simulates the mean velocity shift by increasing the turbulent eddy viscosity in the near-wall region. This correction, usually denoted as High Roughness (HR), has also been extended to the Shear Stress Transport (SST) turbulence model [18] and implemented in widely employed commercial software like Ansys® CFX.

Lastly, a note on roughness influence on heat transfer. The Reynolds analogy is often employed to model heat transfer in gases in proximity of smooth channel walls. Such an assumption is based on the completely similar transport nature of momentum and energy in turbulent flows, both being governed by the same turbulent eddies. Additionally, considering that fluid Prandtl number and Schmidt number are close to unity, the Reynolds analogy can be expressed as shown in Eq. (2.3).

$$C_f/2 = St \tag{2.3}$$

where f is the Fanning friction factor and St is the Stanton number. As a consequence, an increase in friction results in a proportional enhancement of heat transfer. On the other hand, in the fully rough regime, friction drag development and heat transfer processes show substantially different characteristics. Compared to the hydraulically smooth case, while the drag increase is mainly related to pressure forces acting on the roughness asperities, heat transfer enhancement strongly depends on both the fluid-wetted area increment and the augmentation of turbulence levels within the boundary layer [19]. In this regard, an insightful comparison between smooth and rough-wall flows has been carried out by Dipprey and Sabersky [11]. In their experimental study, the channel Stanton number St and fanning friction factor C_f has been tracked for different mass flow rates and surface roughness. Under established fully rough conditions, the friction factor settles to a constant value still higher than that of the smooth case, while the heat transfer decreases monotonically as the Reynolds number increases. This effect becomes more pronounced for channels presenting higher surface roughness elements. Stated differently, the ratio $2St/C_F$ for smooth channels maintains constantly close to unity in the turbulent regime, while for the rough case it decreases to values significantly below 1 with increasing Reynolds number, provided that transition to fully rough conditions occurred. As a result, such a behaviour underlines how the Reynolds analogy emerges as fundamentally inadequate for predicting heat transfer on rough surface.

In light of the intrinsic differences ruling the heat transfer mechanism of flows over rough

surfaces with respect to the momentum transfer, thermal correction models for HR approach have been developed in recent years. Aupoix [19] initially proposed a correction technique based on the turbulent Prandtl number Pr_t, which relates the momentum eddy diffusivity to the energy eddy diffusivity. Its formulation is expressed in Eq. (2.4).

$$Pr_t = Pr_{t,\text{smooth}} + F \exp\left(-\frac{y}{h}\right) \tag{2.4}$$

where $Pr_{t,\text{smooth}}$ is the turbulent Prandtl number for the smooth surface case, F is a maximum-level term attributable to the roughness dynamic effect and related to the mean velocity shift as well as the corrected wetted surface ratio, and the exponential term confines the thermal correction influence within the roughness sublayer accounting for the roughness height h and the wall distance y. Although this approach showed a remarkable improvement in predicting near wall heat transfer, it should be noted that such a correction does not account for fluid properties variations. Other models aims to bridge this gap, focusing especially on embedding the Prandtl number variation influence on F factor formulation. Among these, two similar approaches stand out. Latini et al. [20] focused on deriving a thermal correction model to analyse rough cooling channels in liquid rocket engines. Building on Aupoix's formulation, they employed an in-house developed code plugged with SA HR turbulence model to predict flow behaviour in rough pipes across a wide range of different Reynolds numbers, relative roughness value k_s/D_h and Prandtl numbers. Model calibration has been iteratively performed by adjusting the F factor until the simulated Stanton number matched the one predicted by the Dipprey and Sabersky [11] correlation provided in Eq. (2.5).

$$St = \frac{f/8}{1 + \sqrt{f/8}\left(k_f\left(Re\left(\frac{k_s}{D_h}\right)\sqrt{f/8}\right)^{0.2}(Pr)^{0.44} - 8.48\right)} \tag{2.5}$$

where f is the Darcy friction factor and k_f is a constant characterising quantitively the roughness morphological effect on heat transfer. Dipprey and Sabersky [11], for example, determined a value of 5.19 for roughness elements resembling closely packed sand grains.

Subsequently, Latini et al. [20] elaborated a new Prandtl number-based expression for the definition of F parameter, owing a satisfactory fit with the numerical model calibrated values. Nonetheless, two remarkable considerations should be noted regarding this work. First, their model has been calibrated on data pertaining to closely packed sand grains. Therefore, its performances for other surface morphologies have not been assessed. Moreover, the reference expression Eq. (2.5) used for model calibration, has been derived by

Dipprey and Sabersky [11] under a specific set of assumptions. Firstly, the proposed formulation is limited to the fully rough hydraulic regime, where surface drag is independent of fluid viscosity. Additionally, the so-called cavity vortex hypothesis [11] is assumed to hold. In essence, this hypothesis conceives roughness as a series of small cavities with depth equal to the roughness height. Heat transmitted through the thin boundary layer formed along cavity walls is assumed to be convected by vortices to the cavity opening. By combining the negligible influence of viscosity on pressure drag in the fully rough regime with the cavity-vortex transfer mechanism, it follows that Reynolds similarity can still be considered valid at the cavity openings. Put differently, the roughness height itself can be taken as the reference distance where viscous shear stresses become negligible. One can notice how this hypothesis is at odds with the previously presented roughness sublayer formulation. However, at least for close-packed granular type roughness, this approach yields consistent estimations of the Stanton number as shown both by the corresponding authors and by Latini et al. [20].

Another noteworthy contribution has been provided by Östlund [15], key industrial supervisor of the MERiT project affiliated to GKN Aerospace. Similarly to the approach followed by Latini et al. [20], Östlund developed and compared the accuracy of three in-house thermal correction models named GKN1, GKN2 and GKN3. The additional insight of this work lies in the consideration of different surface topographies during model calibration, which translates into variations of the k_f parameter in Eq. (2.5). For the purposes of the present discussion, only the GKN1 model will be presented hereafter. It essentially consists of a reformulation of the F factor, illustrated in Eq. (2.6).

$$F = g_{2PP} \cdot C(k_s^+)^{\alpha}(Pr)^{\beta}(k_f)^{\gamma} \tag{2.6}$$

where $C = 0.0226$, $\alpha = 0.226$, $\beta = 0.523$ and $\gamma = 1.629$, while g_{2PP} is a piecewise function depending on the local hydraulically rough regime; its definition is provided in Eq. (2.7).

$$g_{2PP} = \begin{cases} 1 & \text{if } k_s^+ \geq 70 \\ \dfrac{\ln(k_s^+) - \ln(5)}{\ln(70) - \ln(5)} & \text{if } 5 < k_s^+ < 70 \\ 0 & \text{if } k_s^+ \leq 5 \end{cases} \tag{2.7}$$

The use of g_{2PP} should compensate for Eq. (2.5) validity in the mere fully rough regime during calibration, consequently correcting the heat transfer for the transitional rough regime and zeroing the F factor for the hydraulically smooth regime.

Despite a reduced accuracy in predicting the Stanton number retrieved through Eq. (2.5) if compared to the other GKN models, GKN1 showed an enhanced robustness when simulations are conducted outside the calibration range, particularly with respect to the Prandtl number. The calibration ranges considered for each parameter in this assessment are reported in Table 2.2.

Parameter	Low limit	High limit
k_s/D_h	0.04	0.21
Pr	0.7	3.35
Re_{D_h}	27356	263678
k_f	5.19	8.0

Table 2.2: Parameters calibration ranges considered by Östlund [15].

Additionally, GKN3 model efficacy has been practically evaluated by simulating the experimental conditions which Stimpson et al. [8] employed in their assessment with a wide set of AM minichannels whose hydraulic diameters vary between 0.415 mm and 1.275 mm. A fine tuning of k_s and k_f parameters has been performed to best match the experimental values of Darcy friction factor and Nusselt number respectively across the investigated Reynolds number range. The k_f values yielding the best fit lay between 4.521 and 8.213, highlighting the substantially different effect of surface roughness morphology on heat transfer, even when all investigated tests articles share the same manufacturing technique. CFD results have generally proved to closely align with the measured values, except for certain test coupon cases where higher geometrical uncertainties may have significantly affected the data employed for model tuning. In conclusion, the findings reported by Östlund [15] provide a valuable evidence for the purposes of the present dissertation: the cavity vortex hypothesis, which Eq. (2.5) stems from, proves suitable to predict the heat transfer in rough AM minichannels, regardless of the morphological effects embedded in k_f parameter and sensed by the fluid flow.

2.3 Methane thermal cracking

Methane thermal decomposition is a highly complex process involving multiple parallel and sequential reactions. Its complete modelling has not yet been fully characterized and lies beyond the scope of the present study. Nonetheless, for the sake of understanding, the compact reaction model introduced by Chen et al. [21] is illustrated as follows:

Initiation step

$$CH_4 \longrightarrow CH_3\cdot + H\cdot \tag{2.8}$$

$$H\cdot + CH_4 \longrightarrow CH_3\cdot + H_2 \tag{2.9}$$

$$2\,CH_3\cdot \rightleftharpoons C_2H_6 \tag{2.10}$$

Secondary reactions

$$CH_3\cdot + C_2H_6 \rightleftharpoons CH_4 + C_2H_5\cdot \tag{2.11}$$

$$C_2H_5\cdot \longrightarrow C_2H_4 + H\cdot \tag{2.12}$$

Tertiary reactions

$$CH_3\cdot + C_2H_4 \longrightarrow C_2H_3\cdot + CH_4 \tag{2.13}$$

$$C_2H_3\cdot \longrightarrow C_2H_2 + H\cdot \tag{2.14}$$

$$CH_3\cdot + C_2H_4 \rightleftharpoons n - C_3H_7\cdot \tag{2.15}$$

$$n - C_3H_7\cdot \longrightarrow C_3H_6 + H\cdot \tag{2.16}$$

It should be noted that the complete reaction network is far more extensive than the scheme presented here and ultimately leads to solid carbon deposition. As can be inferred from the reaction sequence above, methane cracking provides indicators that can be used both during and after testing to assess its occurrence. First, the reduction in methane concentration together with the increase in hydrogen content in the effluent gas can be monitored. Hydrogen formation occurs to a greater extent in Reactions 2.8, 2.9, 2.12, 2.14, and 2.16, and can be detected more readily than other products, providing an early indication of thermal decomposition. Furthermore, the amount of deposited carbon represents an additional indicator of reaction yield, which is influenced by several factors such as pressure and temperature levels, residence time of species under reaction conditions, and the presence of catalytic agents. Depending on the adopted measurement strategy and instrumentation, not all reaction products can be precisely quantified. Nonetheless, by cross-checking the available data, an accurate estimate of methane conversion can be obtained.

In this regard, real-time assessment of the cracking process can be carried out through various approaches, primarily consisting of analysing effluent gas properties. The methods most relevant to the present dissertation are briefly discussed below. Heldens et al. [22] reviewed these measurement approaches in detail and developed an experimental setup to investigate methane thermal cracking and related real-time detection systems. In par-

ticular, Heldens monitored hydrogen concentration in a hot methane flow over Nickel 201 specimens during several isothermal trials at different temperatures and volumetric flow rates. The measurement strategies employed in his work are based on thermal conductivity and speed-of-sound sensor readings for gaseous mixtures, which rely on the following working principles:

- **Thermal conductivity–based sensors**: These sensors typically employ one or more heated elements (e.g., thin wires or MEMS resistive structures). The exposed elements are electrically heated, and heat is dissipated into the surrounding gas. By measuring the heat transfer rate, it is possible to infer the gas thermal conductivity.
- **Speed-of-sound–based sensors**: In these sensors, acoustic waves are generated within a gas-filled cavity using a piezoelectric transducer. The waves propagate over a known path length and are detected by a receiver. By measuring the time of flight of the acoustic signal, the speed of sound in the gas can be calculated.

All other conditions being equal, variations in these properties can then be used to detect changes in gas composition. As previously mentioned, the formation of hydrogen during methane cracking significantly alters the effluent gas properties compared with a pure methane flow. Other hydrocarbon products may also contribute to these variations, making deviations in sensor outputs not easily attributable to the concentration increase of a specific species. Therefore, a quasi-binary mixture model of CH_4 and H_2 has been adopted by Heldens et al. [22] to meaningfully interpret the measured values. This assumption was subsequently validated by analysing the effluent gas composition using a gas chromatograph (GC), which detected no relevant presence of other potentially influencing reaction products. The GC hydrogen concentration output has also been used as a reference baseline to assess the efficacy of these measurement techniques. Despite differences in slope attributable to sensor characteristics and positioning, both strategies showed comparable levels of precision relative to the GC measurements.

The onset of thermal decomposition does not depend solely on temperature but may also be catalysed by the channel material. Higashino et al. [23], for example, experimentally investigated the coking characteristics of several nickel-based alloys used in rocket engines, showing that the catalytic conversion of methane to hydrogen is related to the nickel content of the surrounding material to some extent. Specifically, Inconel 718 (Ni 53.5%), Inconel 600 (Ni 78%), and A286 (Ni 25%) were considered in this work. A set of isothermal trials was conducted with temperatures ranging from 500°C to 850°C, with methane flowing over candidate test specimens. The authors recorded a thermal decomposition onset temperature of approximately 650°C for nickel-based alloys and 800°C for

high-purity (99.9%) methane flow. While this behaviour highlights the partial influence of nickel on methane thermal decomposition onset, it does not exclude the possibility that other alloying elements may also catalyse the reaction. Moreover, Inconel 600 exhibited the highest mean hydrogen inversion rate among the samples across all analysed temperature levels during the initial phases of trials. A comparison of the observed hydrogen inversion rates across isothermal trials is provided in Figure 2.6.

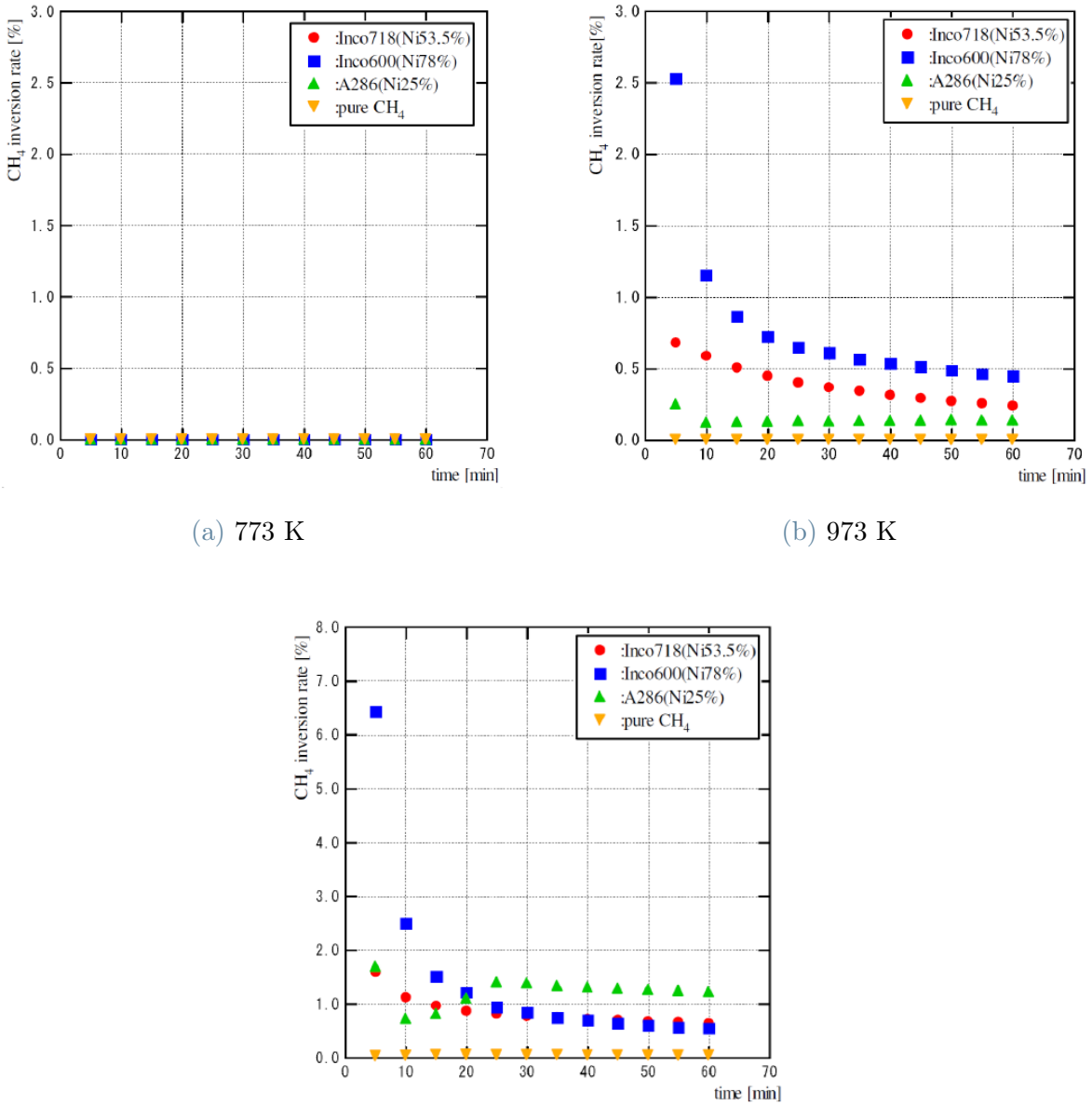

(a) 773 K

(b) 973 K

(c) 1073 K

Figure 2.6: Hydrogen inversion rates comparison between test materials at various isothermal levels. Images from Higashino et al. [23].

As shown in the graphs, nickel content exhibits a proportional relationship with the hydrogen reaction rate. However, at elevated temperatures, hydrogen conversion appears to be increasingly influenced by other mechanisms over extended periods, probably supporting the involvement of additional alloying elements in this process.

In the present dissertation framework, it is reasonable to wonder which influence surface roughness has on the cracking reaction rate as well. In this regard, only a limited number of studies have addressed this topic. Once again, Heldens et al. [24] reviewed these investigations and contributed to expanding the experimental dataset. The authors analysed methane thermal decomposition with Haynes 230 and Inconel 625 samples produced using both additive manufacturing (AM) and subtractive manufacturing (SM) techniques with identical geometrical dimensions. The AM specimen was manufactured using Laser Powder Bed Fusion (LPBF) at an orientation angle of 90°. Samples exhibit similar surface characteristics with an arithmetic mean roughness of $R_a = 11.24\,\mu$m. SM samples, by contrast, are characterized by significantly lower roughness, with $R_a = 0.48\,\mu$m. The same test setup employed in their previous work [22] was used to conduct isothermal tests at fixed pressure and mass flow rate under different temperature levels, with a test duration of 60 minutes. For Haynes 230 alloy, the experimental results showed near-zero hydrogen conversion rates for SM samples at 700°C and 750°C, whereas the AM samples exhibited detectable hydrogen content in the effluent gas over the same temperature range. In particular, trials at 750°C and 800°C revealed a significant increase in reaction rate for AM specimens compared with SM ones, by factors of 8 and 6.7, respectively. Deposited carbon mass was also evaluated by comparing sample weights before and after the trials, confirming the trend observed through real-time measurements, yet presenting some uninterpretable negative values for SM pieces.
The strong dependence between surface roughness and cracking reaction rate is not limited to the aforementioned work but is supported by other experimental studies [25, 26] focusing on different light hydrocarbons. Surface roughness undoubtedly influences the thermal decomposition process. However, as remarked by Heldens et al. [24], the underlying mechanisms responsible for this common trend are not yet fully understood. The increase in coking rate is often attributed to the enlargement of the effective surface area provided by the channel, and thus to an increase in active catalytic sites. This hypothesis is still under investigation and, at present, involves several factors, including geometrical and electronic effects at both macroscopic and atomic scales.

2.4 State of the Art of regenerative cooling experimental facilities

Although methane is not as extensively documented as kerosene-based fuels in regenerative cooling systems, numerous experimental facilities and related studies have been developed in recent years. Most of these aim to investigate cooling performance under transcritical conditions, as this represents a critical design regime. Indeed, when approaching critical conditions, fluids exhibit drastic property variations over a narrow range of pressure and temperature [27]. Typically, in regenerative cooling systems fed with methane, the fluid enters the channels at supercritical pressure and subcritical temperature and is subsequently heated to supercritical temperatures. In proximity to the pseudocritical temperature and pressure, when the fluid is heated at temperatures levels near the critical point, the constant-pressure specific heat exhibits a sharp peak, followed by a rapid reduction in heat capacity as temperature increases [28–30]. This behaviour holds in a lesser extent near the so-called Widom line [27], which represents an extension of the boiling line into the supercritical region where strong thermophysical fluctuations can still be observed. In regenerative cooling systems, this state transition can lead to significant heat transfer deterioration [31, 32], which becomes more pronounced as the fluid approaches the critical point. Unfortunately, the MERiT experimental facility does not include a refrigeration system capable of allowing methane to enter the channel at subcritical temperatures. The minimum achievable inlet temperature is therefore governed by ambient conditions, as methane equilibrates thermally while flowing from the gas packs to the test cell through the external feed line.

Despite the intrinsic differences between the methane flow conditions experienced in the MERiT facility and the transcritical conditions most frequently analysed in the literature, existing experimental facilities for regenerative cooling systems analysis offer a valuable basis for comparison with regard to both instrumentation and analysis methodologies. For example, Votta et al. [33] investigated transcritical methane cooling performance within the HYPROB program, a collaboration between the Italian Aerospace Research Centre (CIRA) and the University of Rome “La Sapienza”. The heated test section closely resembles that employed in the MERiT facility: a GlidCop® Al-15 block equipped with adjustable electrical cartridges heats an integrated rectangular cross-section channel; sets of K-type thermocouples are used to reconstruct the thermal field along the channel wall at different distances from the inner surface; and pressure and temperature sensors measure inlet and outlet conditions. Liquid nitrogen is supplied to a jacketed condensation tank to convert gaseous methane into liquid state before feeding the test section. It is

worth noting the methodology adopted by Votta et al. [33], as it laid the foundation upon which previous assessments within the MERiT programme have been developed [3].
Due to the three-dimensional geometry of the channel and the asymmetric heating conditions, the classical definition of the Nusselt number for a uniformly heated duct, reported in Eq. (2.17), has been deemed not directly applicable.

$$Nu = \frac{\mathrm{HTC} \cdot D_h}{k} \qquad \text{where} \qquad \mathrm{HTC} = \frac{q_w}{T_b - T_s} \tag{2.17}$$

Here, D_h is the hydraulic diameter, k is the coolant thermal conductivity, T_b is the bulk fluid temperature, and T_s and q_w are the inner surface temperature and heat flux, respectively. In one-sided heating configurations, the surface temperature and heat flux vary significantly across a given cross section. Therefore, these quantities are evaluated at a fictitious hot-gas/wall interface located 1 mm below the channel base, representative of a typical rocket engine liner thickness, where they can be considered uniform across the channel width. The heat flux at this interface is obtained from the total electrical power supplied to the heating cartridges, assuming a uniform axial distribution along the channel and negligible heat losses through the insulation. The corresponding wall temperature, instead, is estimated via a one-dimensional conduction model across the wall thickness using those thermocouple measurements closest to the solid-fluid interface. Fluid bulk temperature and thermophysical properties are evaluated at embedded thermocouples stations along the channel axis by assuming linear distributions of enthalpy and pressure. Inlet enthalpy H_i is determined from directly probed inlet conditions, whereas outlet enthalpy H_o is computed from a global energy balance to account for non-uniform temperature distributions at the channel exit section expressed in Eq. (2.18).

$$\dot{m}\,(H_o - H_i) = Q \tag{2.18}$$

where Q is the total heat rate supplied by the cartridges to the channel and retrieved through voltage and current outputs of cartridges transformer, while $\dot{m}$ is the mass flow rate.

Another structured experimental methodology is presented by Haemisch et al. [34] within the DLR Lampoldshausen research group. They investigated heat transfer with cryogenic hydrogen and methane in a subscale combustion chamber equipped with High Aspect Ratio Cooling Channels (HARCC). Their facility integrates multiple diagnostic layers, including mass flow measurements and distributed pressure and temperature sensors positioned along both the feed system and the inlet and outlet manifolds. This measure-

ment system enables the application of a calorimetric approach similar to that employed by Votta et al. [33]. The distinctive feature introduced by Haemisch et al. [34] for the analysis of experimental test conditions lies in an alternative method based on wall temperature reconstruction through an inverse approach. Eighty thermocouples are embedded between adjacent channels at several axial locations and radial depths from the hot-gas side. Thanks to this abundance of temperature measurements, boundary heat fluxes and local heat transfer coefficients can be iteratively optimized until agreement between measured and numerically reconstructed temperatures is achieved in the solid domain, ultimately yielding a quasi-linear hot gas side heat flux distribution for more realistic HTC data processing through CFD simulations.

An additional data-reduction technique is reported in Air Force Research Laboratory investigations on RP-2 cooled channels [35], where heat transfer analysis is deliberately restricted to steady-state and quasi-isothermal operation. Steady-state conditions are assumed once outer wall temperature readings remain within approximately 5% of each other, after which their limited axial variation justifies the assumption of uniform wall temperature. In this case, wetted wall temperatures are not measured directly but are inferred from outer wall data through one-dimensional conduction calculations applied to both directly heated and unheated surfaces. These derived temperatures are then averaged to account for asymmetric heating [35]. The mean convective heat transfer coefficient is evaluated using a log-mean temperature difference formulation reported in Eq. (2.19).

$$\overline{HTC} = \frac{\dot{m}\, c_p}{A_w} \log\left(\frac{T_s - T_{m,i}}{T_s - T_{m,o}}\right) \tag{2.19}$$

where c_p is the constant pressure specific heat of the fluid, while m, i and o subscripts refer respectively mean bulk, tube inlet and tube outlet conditions. Thermophysical properties are evaluated at the mean bulk temperature measured downstream of the heated section, where sufficient mixing ensures representative flow conditions [35]. Experimental conditions of the aforementioned literature assessments are summarized in Table 2.3, together with the employed test article cross section shape and aspect ratio (AR).

Reference	Shape	AR	q [MW/m^2]	T_{in} [K]	p [MPa]	$\dot{m}$ [kg/s]
Billingsley et al. [35]	Circular	–	3–16	∼300	0.5–12	–
Haemisch et al. [34]	Rectangular	1.7–30	11–16	65–140	∼5	–
Votta et al. [33]	Rectangular	3	≤20	130–140	6–15	0.01–0.025

Table 2.3: Experimental conditions investigated in representative regenerative cooling studies.

3 | Experimental facility

The MERiT test infrastructure consists of both hardware and software components. This chapter aims to provide the reader with a sufficiently detailed overview of these subsystems by describing their configuration, equipment, and purpose, in order to enable a clear understanding of the operating conditions under which the tests are performed.

3.1 Hardware and Software equipment

The heated compartment is housed within the test cell shown in Figure 3.1, which encloses the apparatus for safety purposes. During operation, the cell is sealed and continuously supplied with CO_2 to maintain an inert atmosphere. The interior is illuminated and monitored by a remotely controlled dome camera. A differential pressure transducer monitors pressure variations between the inner and outer atmosphere that may indicate a deflagration event occurrence. An internal flammable gas detector is installed to detect hazardous gas concentrations resulting from potential leaks. Two oxygen sensors positioned at different heights monitor O_2 levels to ensure the establishment and maintenance of inert conditions.

Figure 3.1: Test cell.

Pre-trial preparation procedures chronologically consist of:

1. Preparation of the test cell inert atmosphere.
2. Purging of the main CH_4 line with N_2 to remove trapped air from the methane feed and side lines.
3. System pre-heating with flowing N_2 to prevent overheating of components during warm-up.

Methane is stored in a dedicated gas cage connected to the test cell supply line, while nitrogen and carbon dioxide tanks are located in a separate confined compartment. Methane feed piping, certified to withstand pressures up to 200 bar, and nitrogen and carbon dioxide feed piping, certified up to 60 bar, connect the various tanks to the test cell area via the facility roof. The inlet gas flows of methane, main nitrogen, and carbon dioxide are measured using Coriolis-type flow meters, and their mass flow rates are controlled by adjustable Bronkhorst mass flow controllers. Both the main-line mass flow rate and the back pressure are PID-controlled by Bronkhorst E-8000 units in a multichannel configuration. These devices receive mass flow rate and channel inlet pressure signals and actuate regulating valves upstream and downstream of the test section to achieve the desired operating conditions.

During nominal operation, methane flow can be preheated by two ExHeat LTD heaters rated at 35 kW and 9 kW, respectively, in order to set the desired initial flow temperature. The gas then enters the test article, which is mounted onto an oxygen-free (OF) copper block used to transfer heat to the cooling channel. The channel is brazed to the top block using a Cu65Au35 filler alloy to ensure proper thermal contact and promote uniform heat distribution. An underlying copper base block is equipped with 21 electrical cartridge heaters arranged in a 3×7 matrix and connected to a variable transformer capable of supplying up to 400 W each. The base block is directly heated by the cartridges and conductively transfers heat to the upper section. The heating compartment described above, together with the test channel, is insulated with a calcium silicate shell during operation. Heat losses through the insulation range between 2–4% of the supplied power, depending on the coolant mass flow rate [36]. A CAD illustration of the test section is presented in Figure 3.2.

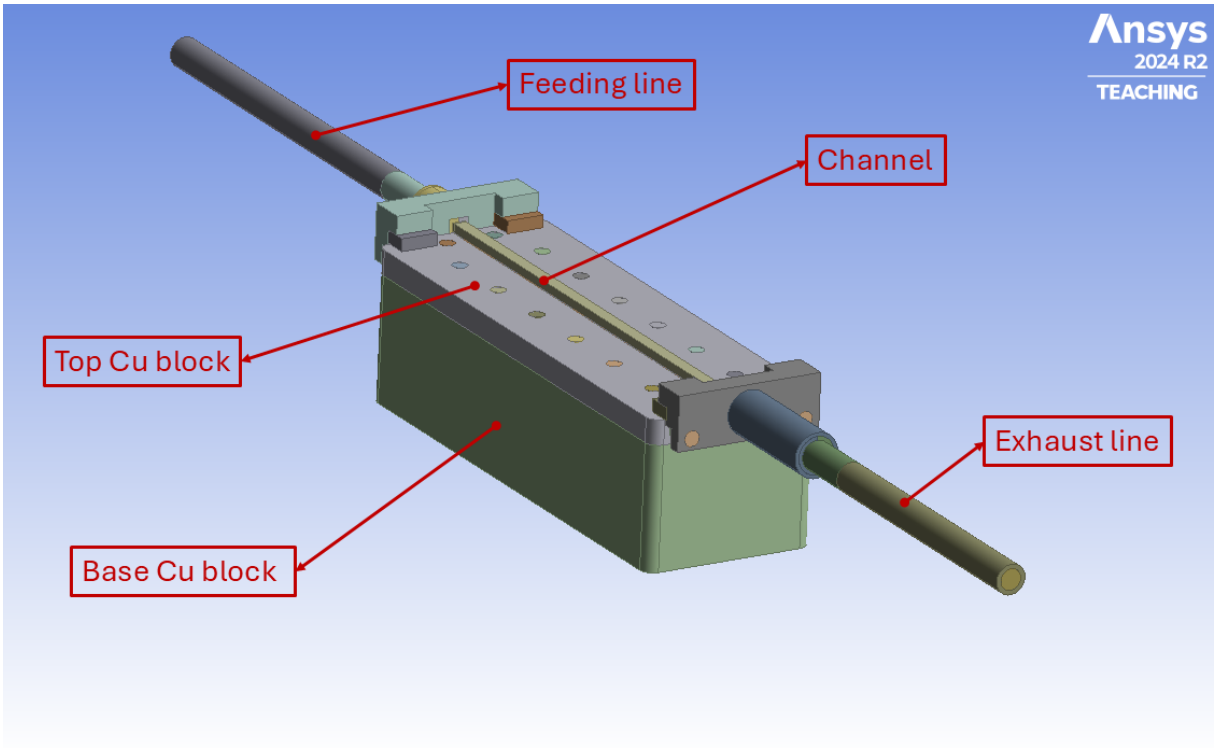

Figure 3.2: Test section CAD (Ansys Design Modeller).

Further downstream of the heater assembly, the methane flow is cooled by means of a heat exchanger and its pressure is reduced through a series of reduction valves. This process lowers the temperature and pressure to safe levels, allowing the flow to be flared through an Euromekanik AB system. The adopted exhaust disposal system has been deemed necessary to minimize the environmental impact of operations. Downstream of the heat exchanger, a sampling port is installed on a dedicated bypass line. This line enables real-time assessment of methane thermal decomposition using Optel Optim 2.0 and Xensor XEN-5320 sensors, which operate on speed-of-sound and thermal-conductivity measurement principles, respectively.

With regard to the measurement system, numerous sensors are deployed at critical locations to monitor operations and to collect data for subsequent processing. Their most relevant features are described hereafter, with particular emphasis on the test section layout, which is of primary importance for data extrapolation.
A longitudinal symmetry section of the heating compartment is illustrated in Figure 3.3, and sensor locations are provided relative to the channel inlet according to the reference system shown. The X, Y, Z coordinates are normalized by the channel length, height, and width, respectively, and are reported in Table 3.1.

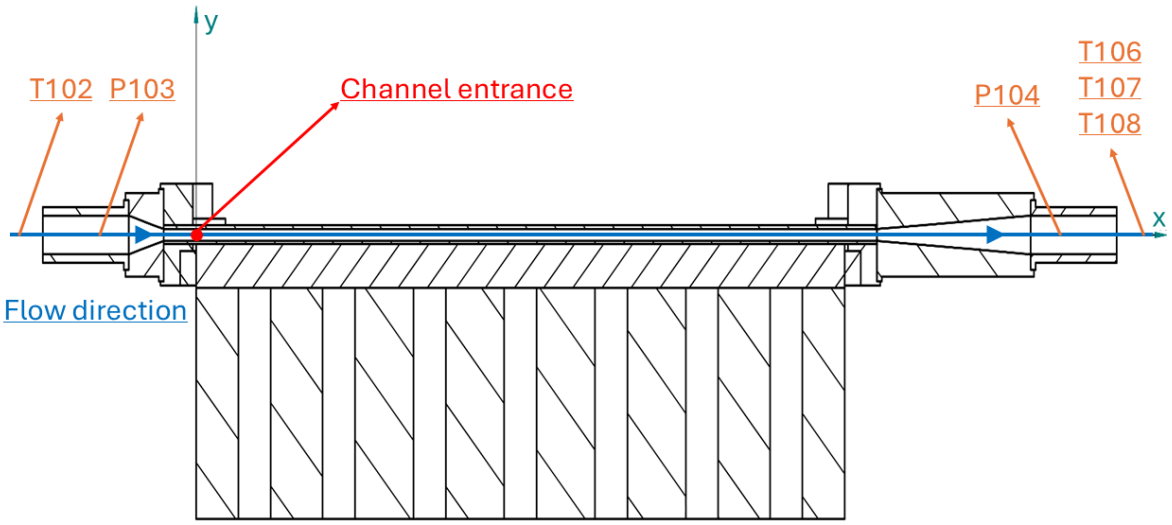

Figure 3.3: Heating compartment longitudinal section (not to scale).

Sensor ID	X	Y	Z
TWC301	0.01	0.77	0
TWC303	0.185	0.77	0
TWC305	0.5	0.77	0
TWC307	0.82	0.77	0
TWC309	0.99	0.77	0
TWH301	0.01	-0.75	0
TWH302	0.15	-0.75	0
TWH304	0.43	-0.75	0
TWH306	0.57	-0.75	0
TWH308	0.85	-0.75	0
TWH309	0.99	-0.75	0
TWM313	0.185	0	-0.83
TWM323	0.185	0	0.83
TWM315	0.5	0	-0.83
TWM325	0.5	0	0.83
TWM317	0.82	0	-0.83

(a) Channel temperature sensors.

Sensor ID	X	Y	Z
TEH303	0.185	-1.23	0
TEH305	0.5	-1.23	0
TEH307	0.82	-1.23	0

(b) Copper block temperature sensors.

Sensor ID	X	Y	Z
T102	-0.75	0	0
T106	1.91	1.06	0
T107	1.91	0	0
T108	1.91	-1.06	0

(c) Inlet and outlet temperature sensors.

Sensor ID	X
P103	-0.34
P104	1.49

(d) Inlet and outlet pressure taps.

Table 3.1: Normalized sensors locations.

The inlet and outlet pressures are measured at locations P103 and P104, listed in Table 3.1d, respectively upstream and downstream of the inlet nozzle and outlet diffuser connecting the feed and exhaust lines to the test article. Similarly, the corresponding temperatures are measured at T102 and at T106, T107, and T108. The latter three sensors are configured as a temperature rake, with T106 at the top and T108 at the bottom, allowing proper detection of temperature stratification resulting from the one-sided heating configuration. Several K-type thermocouples are installed along the channel and are designated as TWC, TWH, and TWM in Table 3.1a. These sensors measure temperature at different longitudinal stations: the TWH set is located at the solder interface in proximity of the channel base; TWC measures temperatures along the upper portion of the channel; and the TWM set probes temperatures along the lateral channel walls. TWH thermocouples feature a specific configuration. Typically, K-type thermocouples measure temperature through the Seebeck effect generated between a cold and a hot junction formed by Nickel–Chromium and Nickel–Alumel wires. In this case, the hot junction ends do not directly connect but are brazed onto the channel base sides, interfacing with the solder layer. The presence of the channel alloy at these junctions can be accounted for through appropriate calibration. Given the symmetric configuration, their close proximity to the assembly symmetry plane, and the presence of a solid copper layer promoting heat spreading, the temperature difference between the two junction points is assumed to be negligible. Additionally, thermocouples insulating shell prevents localized cooling effects around these connections. The TEH sensor set reported in Table 3.1b refers to thermocouples installed from the block side in small drilled holes within the copper base block near the solder interface. Figure 3.4 shows the channel mounted on the base block together with the thermally shielded thermocouple wiring.

A Yokogawa EJX 530A pressure transmitter is connected to P103 location and a Yokogawa EJX 110A differential pressure transmitter is connected to both P103 and P104 locations. The mass flow is measured by a Rotamass Nano flow meter of the same brand. As previously mentioned, the mass flow and P103 outputs are fed into the PID controller which actuates control valves up and downstream of the test section such that both mass flow and inlet pressure can be actively controlled by the operator.

All sensors and actuators are connected to a NI CompactRIO (cRIO) modular system which interfaces with a local terminal. The data acquisition rate configured on the cRIO is set to 10 Hz. Set points are recorded over a 90 s interval, allowing the calculation of both the mean value and standard deviation for each test condition. A detailed description of the considered test conditions is given in Section 4.2. The NI modules locally interact with a suited LabVIEW environment loaded on the terminal allowing the operator to

command system actions, monitor sensors outputs and system status as well as log data.

Figure 3.4: Configured test rig.

3.2 Test article and Roughness characteristics

The experimental campaign was conducted using a specific configuration of the test article provided by GKN Aerospace. It consists of a rectangular cross-section minichannel additively manufactured (AM) by laser powder bed fusion (LPBF) in Haynes 230 alloy. Its nominal hydraulic diameter amounts to 2.915 mm. A longitudinal section view of the channel is shown in Figure 3.5, while Table 3.2 reports the chemical composition of Haynes 230.

Figure 3.5: Channel longitudinal section (not to scale).

The build orientation was set at 90° with respect to the printing bed, allowing the channel to extend vertically along its length. This feature, together with the manufacturing process, is strongly related to the roughness height of the channel inner walls. According

Element	Weight %
Nickel	≈57
Chromium	22
Tungsten	14
Molybdenum	2
Iron	3 max.
Cobalt	5 max.
Manganese	0.5
Silicon	0.4
Niobium	0.5 max.
Aluminium	0.3
Titanium	0.1 max.
Carbon	0.1
Lanthanum	0.02
Boron	0.015 max.

Table 3.2: Nominal chemical composition of Haynes 230 alloy [37].

to Stimpson et al. [8], a vertical build orientation reduces wall roughness compared with shallower build angles due to the absence of downward-facing surfaces.
Other factors significantly affect surface roughness along the channel length, as reported by Raj et al. [38], whose work pertained to the MERiT project as well. As a researcher actively involved in the project, Raj characterized the inner surface roughness of the same channel configuration employed in the present experimental trials and highlighted the relatively coarse surface morphology of the specimen. Areal roughness parameters were measured in six spots at a representative position where the flow can be assumed fully developed. In particular, the arithmetic mean height S_a, the root mean square height S_q, skewness S_{sk}, and kurtosis S_{ku} were obtained through white-light interferometry analysis. The S_a and S_q values range between 12–19 μm and 15–23 μm, respectively. Skewness varies between positive and negative values, highlighting the heterogeneous morphology of the surface, while S_{ku} remains close to 3, indicating moderately pronounced peaks in some specimens without evidence of extreme spikiness overall. Furthermore, Raj et al. [38] investigated test article roughness friction characteristics through both experimental measurements and analytical evaluation. Nitrogen cold-flow tests were conducted to monitor the pressure drop across the channel over a mass flow rate range between 3 kg/h and 33.5 kg/h. Considering Darcy friction factor values under fully developed turbulent flow

conditions, a k_s/D_h value of approximately 1.95 was obtained, corresponding to a mean equivalent sand-grain roughness of 39 μm. This value was derived using a wetted perimeter obtained from optical microscopy measurements, which proved to differ significantly from the nominal value. The perimeter tracked through the aforementioned approach, in fact, accounts for surface asperities contributions in both the computation of cross section area and internal perimeter, yielding an hydraulic diameter of 1.996 mm. In addition, comparison with a calibrated numerical model confirmed the consistency of the estimated k_s value, as similar pressure drops were predicted by CFD simulations. In their numerical analysis, roughness effect on fluid flow were modelled through a wall-function-based modelling rather than HR approaches described in Section 2.2, targeting a wall adjacent cell height y^+ value of 50.

4 | Methodology

In light of the previously described analysis framework and the stated research objectives, an appropriate approach should be implemented to account for the various features of the analysed test article configuration. As previously mentioned, the goal of the experimental trials is to assess the heat transfer performance of the AM channel through the available set of sensors in the test rig. To this end, an estimation of the heat transfer coefficient (HTC) at the different thermocouple measurement stations is required. Moreover, the existing numerical model developed by Ristic [1] and refined by Pettersson [2] should be updated to include the effects of the channel surface roughness on the mean flow. CFD simulations will provide a meaningful means of comparison to evaluate the effectiveness of the experimental data processing. The following sections present a detailed description of the methodologies adopted for both the experimental approach and the numerical investigation.

4.1 Experimental Model

The previous experimental model for MERiT data processing developed by Heldens et al. [3] closely resembles the model discussed in Section 2.4 by Votta et al. [33]. However, several differences between the two approaches should be highlighted. Firstly, Heldens retrieved the Nusselt number using the classical definition presented in Eq. (2.17). To this end, the wetted surface temperature was computed by assuming a constant heat flux along the channel length and applying a one-dimensional heat conduction model through the channel base thickness to propagate TWH temperature measurements at the channel base at the channel inner surface. Due to the unavailability of cartridge heater power measurements in the MERiT facility, the total heat rate through the channel base interface was determined from the energy balance defined in Eq. (2.18), considering the inlet temperature and the mean outlet temperature measured by the three rake probes. Unlike the setup described by Votta et al. [28], temperature non-uniformity at the channel exit section is partially captured in the MERiT rig, thereby enhancing the reliability of the energy balance in obtaining a representative value for the fluid heat pick-up. The total heat

flux q_w was then obtained by dividing this value by the channel base surface area. Strictly speaking, this approach should account for total temperature in compressible fluid flows. In practice, the thermocouples used to measure the fluid temperature are configured such that the flow stagnates around the hot junction, thereby returning total temperature values. Regardless of this consideration, as supported by numerical analysis, the differences between static and total temperatures at the feed and exhaust line sections are negligible. The temperature probes are located along these lines, which have a significantly larger cross-sectional area than the test article channel. In these regions, the fluid velocity is considerably lower. If the Mach number at these measurement locations remains below compressible flow threshold [1], the difference between total and static temperatures results negligible.

Similarly to the approaches by Votta et al. [28] and Billingsley et al. [35], channel inner wall temperatures can be obtained from TWH readings through a one dimensional conduction model by using Eq. (4.1).

$$T_s = T_{TC} - \frac{q_w \, t_{wall}}{k_{wall}} \tag{4.1}$$

where q_w is the heat flux, t_{wall} is the test article base thickness, k_{wall} is the material thermal conductivity, and T_{TC} is the thermocouple reading. Thermal conductivity is well known to be temperature dependent. In the present framework, the aforementioned parameter evaluated at the sensor temperature level has been adopted for thermal propagation. The assumption of constant thermal conductivity for heat conduction has been previously compared with a variable thermal conductivity model to evaluate its reliability. Figure 4.1 compares the one-dimensional temperature profiles obtained under the two assumptions across the channel base thickness. Representative values of heat flux and sensor temperatures measured in the experimental rig were employed as boundary conditions.

[1] Significant compressibility effects typically arise for Mach numbers above 0.3.

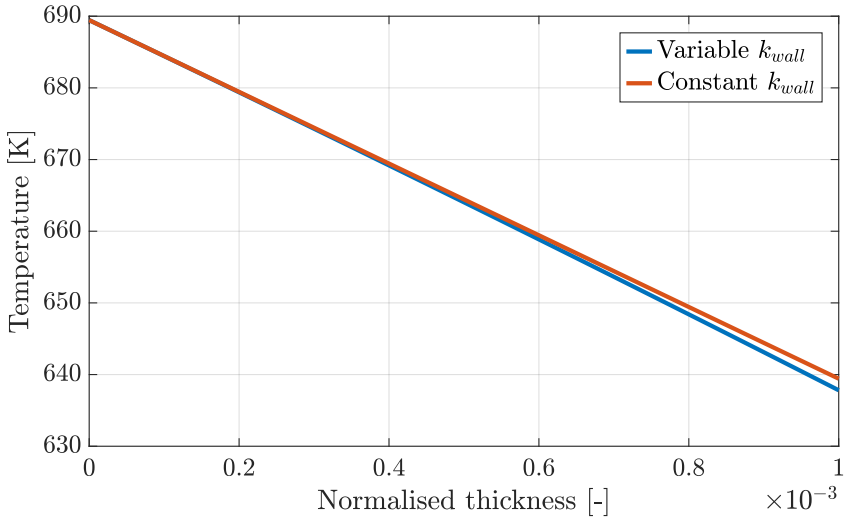

Figure 4.1: Temperature profile across the channel base thickness considering constant and variable wall conductivity for Haynes230.

As observed, the final temperature values predicted by the two approaches differs by 1.6 K, highlighting a reasonably negligible discrepancy if related to the overall temperature decrement. It must be noted that, according to the employed methodology, the whole temperature increment experienced by the fluid across the channel and consequently the thermal energy supply is modelled such that it occurs entirely through the channel base. Surely, this heat transfer representation does not match real test conditions, especially for relatively high cartridges power supply, for which temperature decrement across the channel thickness would be reasonably less pronounced. On the other hand, referring directly to T_s temperatures enables a more consistent comparison of the estimated Nusselt and Stanton number with existing semi-empirical correlations. Since the experimental coefficients will be employed for the selection of some thermal correction parameters in the numerical model, the aforementioned definition of HTC has been chosen as reference in the present experimental scenario.

The TEH sensors provide additional locations from which HTC values can be derived. The previously described one-dimensional heat conduction approach can still be applied, given their embedded position within the copper block. In this case, Eq. (4.1) is used to determine the temperature at the interface between the top copper block and the channel base, accounting for the thickness separating TEH thermocouples and the channel external surface. The interface temperature is then corrected by including the additional thermal contact resistance introduced by the solder layer. The corrected value is subsequently propagated through the wall thickness to obtain the inner surface temperature at these stations. Due to additional elements involved in this estimation procedure, sur-

face temperatures derived from TEH measurements exhibit a higher degree of uncertainty compared with those obtained from the TWH sensors. A schematic illustration of the temperature propagation process is provided in Figure 4.2.

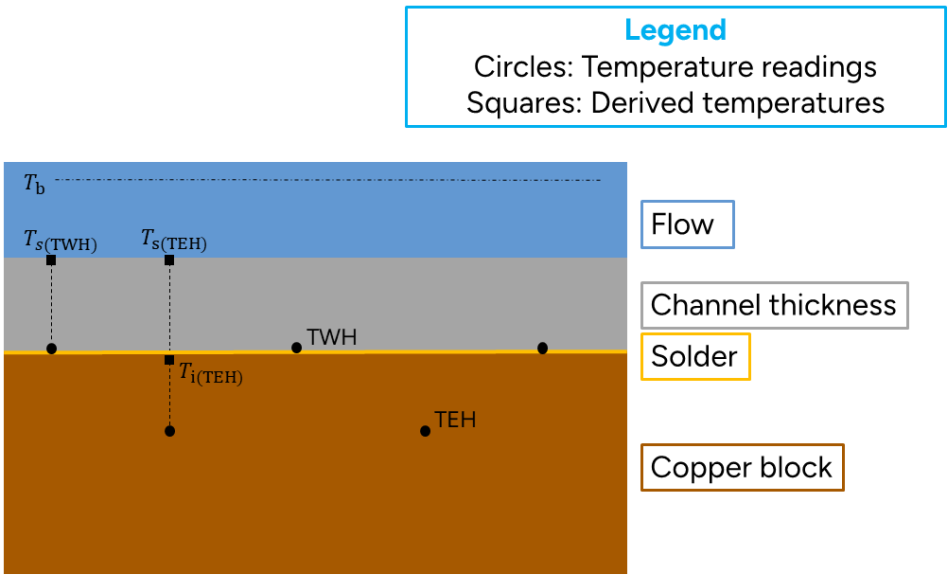

Figure 4.2: Temperature propagation illustrated for TWH and TEH thermocouples.

The definition of HTC and Nusselt number in Eq. (2.17) requires an estimation of the fluid bulk temperature at the same station where the surface temperature is evaluated. The fluid temperature along the channel varies according to the flow conditions experienced over the test article length. Within the present experimental framework, friction, heating, and compressibility effects significantly influence both pressure and temperature distributions, which cannot be reliably described using simplified quasi one-dimensional approaches such as Rayleigh or Fanno flow approximations, owing also to the three-dimensional characteristics of the flow. Furthermore, measuring pressure and temperature using intrusive probes in confined flows such as minichannels is strongly discouraged, as these elements would introduce substantial disturbances to the mean flow, yielding a remarkably different flow state with respect to the actual operating conditions of the system. Consequently, in the MERiT experimental facility, flow variables need to be estimated from sensor measurements located upstream and downstream of the test section. The model implemented by Heldens et al. [3] assumed a linear interpolation of pressure between P103 and P104 pressure taps, as well as a linear interpolation of temperature between the value measured by sensor T102 and the average of the three temperature

rake sensors T106, T107, and T108. Since these measuring stations are located along the pipeline, the effects of the inlet nozzle and the outlet diffuser, which connect the test article to the feed and exhaust lines, were not accounted for. These components may reasonably exert a significant influence on fluid variables variations, particularly when dealing with gases exhibiting notable compressibility effects. In light of these considerations, the methodology adopted in the present study aims to refine the previously developed model by incorporating the influence of these connections. To this end, a straightforward approach based on established correlations for compressible flow has been implemented. First, the Mach number immediately downstream of the inlet nozzle and upstream of the outlet diffuser was determined under isentropic flow and perfect gas assumptions using the area–Mach number relation reported in Eq. (4.2), having available the inlet and outlet conditions obtained from the sensor measurements.

$$\frac{A}{A^*} = \frac{1}{M_{ise}} \left[\left(\frac{2}{\gamma + 1} \right) \left(1 + \frac{\gamma - 1}{2} M_{ise}^2 \right) \right]^{\frac{\gamma+1}{2(\gamma-1)}} \tag{4.2}$$

where M_{ise} is the Mach number at the station presenting a cross-sectional area A under isentropic assumptions, γ is the ratio of specific heats of the gas, and A^* is the critical area at which sonic conditions are reached. The value of γ, as well as the other fluid properties mentioned hereafter, are obtained from the CoolProp 7.2.0 database, which accounts for real-gas model. Subsequently, the isentropic pressure at the same locations can be expressed as shown in Eq. (4.3).

$$\frac{p_0}{p_{ise}} = \left(1 + \frac{\gamma - 1}{2} M_{ise}^2 \right)^{\frac{\gamma}{\gamma-1}} \tag{4.3}$$

where p_0 is the total pressure and p_{ise} is the isentropic static pressure at the same station. Owing to the pronounced roughness effects in these connecting elements, the assumption of isentropic pressure change through the connecting elements may introduce significant errors. To address this issue, a correction to the previously estimated pressure values was applied. By referring to the experimental pressure drop measurements reported by Raj et al. [38] for the same test article configuration, which were kindly shared with the author, the concentrated pressure losses occurring in the nozzle and diffuser were quantified. Specifically, concentrated friction losses for incompressible flow can be expressed as shown in Eq. (4.4).

$$\Delta p_f = \frac{1}{2} \rho v^2 K \tag{4.4}$$

where ρ is the fluid density, v is the flow velocity, and K is the resistance coefficient. According to the Crane manual [39], these parameters may be defined at either the inlet or the outlet of a pipe contraction or enlargement. If the K value is referred to the smaller diameter section, it can be converted to the larger one dividing it by $\beta^4 = (D_s/D_l)^4$, where the subscripts s and l denote the smaller and larger diameters, respectively. The nitrogen cold-flow trials were conducted under incompressible flow conditions. Therefore, the resistance coefficient in Eq. (4.4) can be obtained directly by subtracting the static pressure variation associated with the cross-sectional area change from the total static pressure difference measured between the inlet and outlet of the element. The cold-flow apparatus includes pressure taps located immediately upstream and downstream of these connecting elements, enabling direct measurement of the overall pressure variation. Figure 4.3 presents the experimental K values referred to the smaller section of the element for cold-flow cases at different Reynolds numbers, provided that fully turbulent flow conditions are achieved.

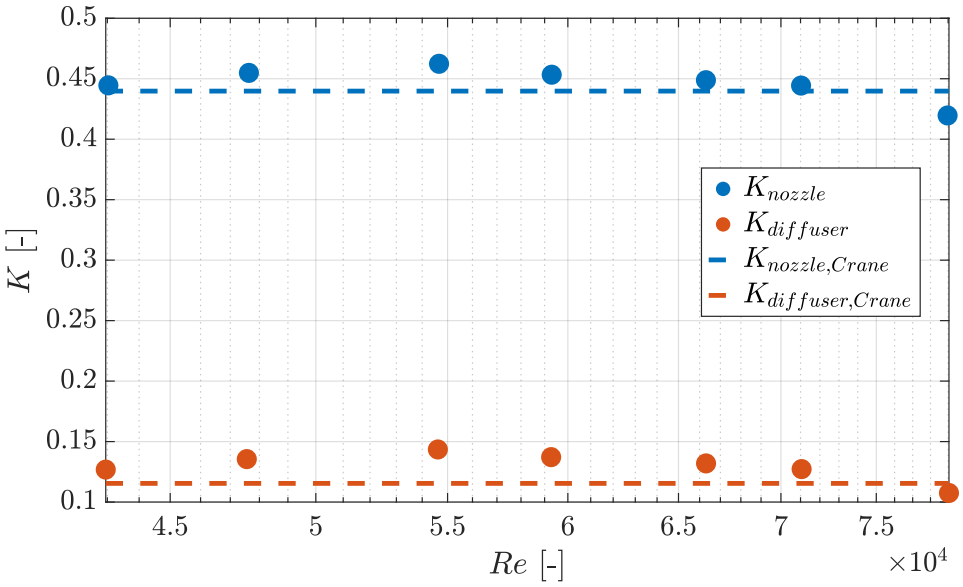

Figure 4.3: Experimental resistance coefficients K compared to theoretical values for fully turbulent regimes from Crane manual [39] (Reynolds number refers to the larger diameter section).

Figure 4.3 also includes theoretical K values reported in the Crane manual for a sudden contraction and a gradual enlargement of a pipe under fully turbulent conditions, respectively. The rationale for selecting a sudden contraction as a reference for the inlet nozzle lies in the fact that, unlike the gradual slope characterizing the diffuser, the inlet contraction occurs over a relatively short axial length comparable to the larger diameter section.

This suggests that the nozzle behaviour is closer to that of a sudden contraction, despite the progressive transition provided by the element geometry. It should also be noted that the K parameter is not entirely independent of the Reynolds number. However, it tends to approach a constant value at sufficiently high flow velocities [40], following a trend similar to that of Darcy friction factor as Re increases. The Reynolds number experienced by methane in the feeding line are approximately equal to or higher than the maximum values investigated by Raj et al. [38], from which the experimental K values were derived. Consequently, even with identical fitting geometries, the resistance factor applied to the MERiT configuration may lead to an overestimation of frictional pressure losses.
Since, in the present set-up, the known flow conditions refer to the larger line sections, an appropriate conversion of the K values is required. Following the Crane manual approach, the resistance factor are then converted to the larger feed line diameter section. Consequently, the friction losses in the MERiT test section fittings can be retrieved from the available inlet and outlet sensor readings. In this case, an average of the experimentally derived K values in Figure 4.3 was adopted to evaluate Δp_f. It should also be noted that compressibility effects may influence friction losses. When Δp_f exceeds 10% of the upstream pressure, a correction based on the net expansion factor Y for compressible flow should be considered [39]. For the experimental conditions analysed in the following sections, Δp_f was found to be well below this threshold for both the nozzle and the diffuser. Consequently, this adjustment was neglected in the present work. However, it should be included in cases where larger pressure drops occur in this fittings. The overall pressure drop across the connecting elements is then obtained as presented in Eq. (4.5).

$$\Delta p = \Delta p_{ise} + \Delta p_f \tag{4.5}$$

Once the pressure values immediately downstream and upstream of the inlet nozzle and outlet diffuser respectively, have been corrected, the corresponding temperature values can be determined by assuming adiabatic flow across the fittings. Considering the close proximity of these elements to the heating compartment, this assumption may be questionable, particularly when high heat power levels are supplied to the test section. Nonetheless, owing to their limited axial length compared with the channel and to the insulation layout surrounding the fitting sections, the resulting temperature variation estimated through this approach may still be considered reasonable. The validity of this modelling assumption cannot be verified through the available experimental measurements. Therefore, further assessment should be carried out through numerical analysis. Under this hypothesis, the effective Mach number M at the channel ends can be obtained from Eq. (4.6)

[41].

$$\frac{\dot{m}}{A} = \sqrt{\frac{\gamma}{R}} \frac{p}{\sqrt{T_0}} M \sqrt{1 + \frac{\gamma - 1}{2} M^2} \tag{4.6}$$

where $\dot{m}$ is the mass flow rate, R is the specific gas constant, p is the corrected pressure obtained through Eq. (4.5), and T_0 is the total temperature, which remains constant across the fitting under adiabatic flow conditions. Subsequently, the static temperature at the corresponding stations can be directly derived using Eq. (4.7).

$$\frac{T_0}{T} = \left(1 + \frac{\gamma - 1}{2} M^2\right) \tag{4.7}$$

Having determined the pressure and temperature values at the channel boundaries, modelling the variation of fluid properties along the channel length remains a challenging task. Under the present experimental conditions, where both friction and heat transfer significantly influence compressible flow behaviour, the fluid evolution cannot be reliably captured through purely analytical approaches. In addition, entrance effects associated with the transition from the larger upstream line to the channel through the inlet nozzle introduce further complexity. In light of these considerations, a linear interpolation of the fluid variables between the channel ends, as adopted by both Heldens et al. [3] and Votta et al. [33], has been applied. It should be noted, however, that this approach neglects the non-linear trend of the Mach number along the channel, particularly when significant friction losses and heat fluxes are present, potentially leading to choked flow conditions. Since the heat input can be regulated in the test rig, it may be set to sufficiently low levels to prevent excessive Mach number growth. With regard to the friction factor associated with surface roughness, the experimental and numerical investigations by Raj et al. [38] indicate that Darcy friction factor is not expected to reach extreme values, remaining approximately on the order of 0.05 for fully developed fluid stations. However, it is reasonable to inquire how compressibility effects may influence pressure decay, particularly when coupled with the rough surface morphology of the channel. The pressure drop surely differs differ between methane and nitrogen flows due to the different density and velocity levels characterizing the two fluids in the two different test conditions. On the other hand, as noted by Shapiro [41], for fully developed flow conditions the influence of Mach number on the observed Darcy friction factor is negligible as long as the flow remains subsonic. For the present test article configuration, if pressure losses were to lead to choking, sonic conditions would occur near the channel outlet, immediately before the diffuser inlet, ensuring that all upstream stations remain subsonic. Consequently, the incompressible

friction factor values reported by Raj et al. [38] are expected to be representative of those experienced in the MERiT apparatus regardless of the channel outlet Mach number, at least within the fully developed flow region.

4.2 Test plan

Given the objectives of the present analysis, a suitable test plan was developed to enable a meaningful comparison between experimental and numerical results within the proposed theoretical framework. Three trials were conducted sequentially while maintaining the test article configuration unchanged:

- **Trial 1**: Conducted with low heat input to the channel to avoid the onset of thermal cracking and to provide an unambiguous assessment of system performance under nominal operating conditions. The pre-heaters were set to 275 °C and 295 °C, and the main heater power was set to 14% of its maximum capacity, resulting in heat flux values between 1.10 and 1.28 MW/m^2.
- **Trial 2**: Performed with higher heat input and extended test duration to promote methane thermal decomposition and carbon deposition on the inner surface, thereby enabling a quantifiable evaluation of heat transfer deterioration. A stable final heater setting was achieved through continuous adjustment of the input power, constrained by the maximum allowable electrical cartridge temperature of approximately 800 °C. The lowest achievable methane mass flow rate was maintained throughout the test duration of approximately one hour. This strategy was adopted to maximize methane residence time within the channel, thereby enhancing thermal decomposition and improving chances for both its real time detection and test conditions comparison with trial 3 outcomes.
- **Trial 3**: Designed to reproduce the operating conditions of Trial 1 while preventing further carbon deposition, thereby enabling a meaningful comparison between the eventually coked and clean configurations.

For the first and third trials, a sufficiently wide range of mass flow rates was considered necessary to investigate methane cooling performance over different Reynolds numbers. Six test points were achieved during each trial, with the back-pressure regulation valve fully open. Considering the data acquisition frequency of the measurement system, each test point represents the average of 900 samples collected under stable operating conditions. The achieved test points are listed in Table 4.1 and Table 4.2, together with the channel average Reynolds number, inlet temperature, and pressure recorded during the

experimental runs.

Test point ID	**Average *Re*** [-]	T_{in} [K]	p_{in} [bar]
1	1.53×10^5	606.27	16.38
2	1.92×10^5	606.82	20.94
3	2.89×10^5	602.28	32.07
4	3.93×10^5	586.05	42.83
5	4.99×10^5	573.51	53.53
6	5.99×10^5	565.84	63.68

Table 4.1: Test matrix for the 1st trial.

Test point ID	**Average *Re*** [-]	T_{in} [K]	p_{in} [bar]
1	1.54×10^5	604.53	16.13
2	1.91×10^5	608.64	20.59
3	2.87×10^5	602.28	31.70
4	3.94×10^5	583.56	42.07
5	5.00×10^5	568.38	52.35
6	6.03×10^5	563.68	62.77

Table 4.2: Test matrix for the 3rd trial.

Since the pre-heaters regulating the test section inlet temperature exhibit significantly higher thermal inertia compared with the final heater, achieving identical inlet temperatures in separate trials is hardly feasible. Consequently, discrepancies of up to 5 °C for the same test point between the first and third trials may be observed.

4.3 Numerical Model

Due to the uncertainties associated with the experimental data reduction model, a meaningful comparison with numerical simulations can provide a more complete representation of the fluid field at the investigated operating conditions. CFD undoubtedly represents a powerful tool for test rig characterization under prescribed boundary conditions. However, it also entails its own set of uncertainties and limitations. In light of these inherent

constraints within the present study framework, this chapter does not aim to provide a comprehensive review of the theoretical foundations of the employed methods. Instead, it focuses on their key features and the most relevant physical implications. Accordingly, the principal observations derived from the CFD model will be highlighted and subsequently compared with the experimental results. As a result, the methodology adopted in this work is not limited to the analysis of physically measured parameters but extends to a mutual validation of the experimental and numerical models.

The numerical framework adopted in the following analysis is based on a conjugate heat transfer model implemented in Ansys® CFX, previously developed by Ristic [1] and Pettersson [2]. The meshed assembly includes mechanical constraints such as clamps used to secure the test article to the base block, fastening screws, and both the inner and outer insulation layers. Minor geometric simplifications were introduced to facilitate meshing without altering the overall thermal response of the system. A visual representation of the computational domain is provided in Figure 4.4.

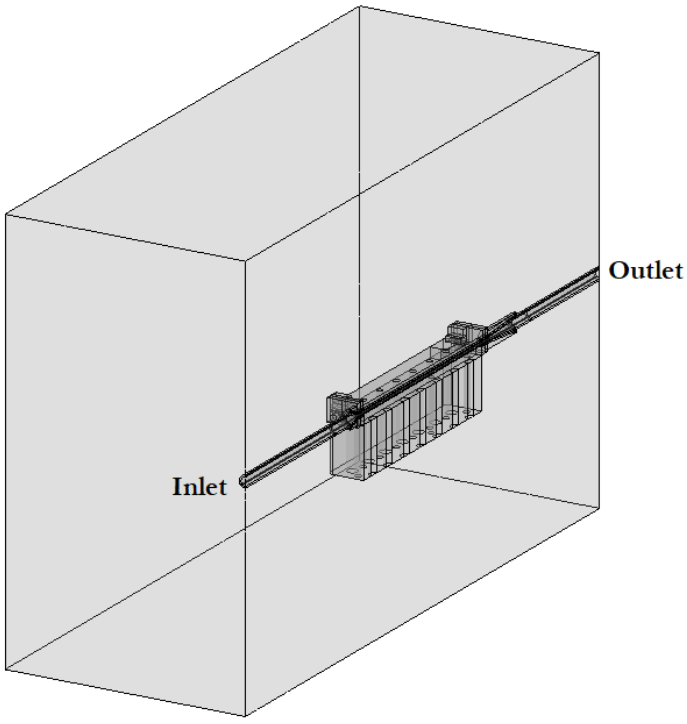

Figure 4.4: Computational domain. (Image from Pettersson [2]).

The fluid was modelled as a continuous compressible medium using the total energy formulation. Methane thermophysical properties were retrieved from real-gas lookup tables,

whose limits were defined in accordance with the experimental operating range, including an appropriate margin. Solid regions were assigned material properties corresponding to the copper blocks, the Cu65Au35 solder layer, and other metallic alloys composing the channel clamp. The Shear Stress Transport (SST) turbulence model was selected due to its ability to maintain accuracy in the near-wall region while preserving robustness in the core flow. Buoyancy effects were neglected owing to the dominance of forced convection within the channel. A low-Reynolds-number near-wall treatment was employed, targeting dimensionless wall distances below unity to ensure that heat transfer is directly resolved rather than modelled through built-in wall functions. To achieve this, inflation layers were introduced along the channel walls to capture steep temperature gradients, while local mesh refinement was applied at the feeding line–channel junctions, where strong velocity gradients are expected. The mesh was generated by decomposing the geometry to enable predominantly swept elements across the fluid domain and the main structural components. Non-conformal interfaces between selected bodies were treated using General Grid Interface connections to preserve flux continuity. Mesh adequacy was subsequently verified through mesh independence studies and solver precision comparisons.

The adaptation of the previously developed numerical model to rough channels mainly consisted of implementing surface roughness through the equivalent sand-grain roughness approach and introducing a thermal correction model for rough surfaces. As discussed in Section 2.2, the High Roughness approach in CFX provides an effective means of predicting the increased turbulence levels in the near-wall region and the associated roughness-induced pressure drop increment. First, an appropriate k_s parameter has been selected based on the work of Raj et al. [38]. In that study, the equivalent sand-grain roughness has been derived using a hydraulic diameter evaluated through white light interferometry, accounting for surface asperities in the wetted perimeter calculation. In the present numerical framework, a different approach has been adopted by referring instead to the nominal hydraulic diameter. In light of this difference, the equivalent surface roughness proposed by Raj et al. has been corrected, yielding a value of approximately 57 μm and applied to the test article-fluid interface, while keeping the feed and exhaust line inner walls as smooth surfaces. The selection of such a parameter has been subsequently verified by comparing the experimental pressure drop realised between P103 and P104 locations and the ones predicted through the HR approach for test point 1.
In addition, GKN1 thermal correction model has been adopted, both for ease of implementation through CFX Expression Language (CEL) and for its enhanced robustness outside the calibration range considered by Östlund [15] as well as its proved efficacy in predicting heat transfer coefficients for minichannel configurations. The relative roughness associ-

ated to the corrected k_s and nominal hydraulic diameter is approximately 0.0195 which lies outside the limits reported in Table 2.2. Accordingly to most practical engineering applications, the smooth-wall turbulent Prandtl number in Eq. (2.6) has been fixed to 0.9 [15]. With regard to k_f parameter, which embeds the influence of roughness topology on heat transfer, a value of 5.19 has been adopted. The rationale behind these choices will be clarified in Chapter 5, owning to the experimental methodology related limitations. In light of roughness treatment in CFX [42], the inflation layers in the fluid domain have been slightly modified so that the first layer is located at half the equivalent roughness height. Surface roughness produces an effective blockage effect on the flow of approximately 50% of its height. Consequently, the computational wall is displaced at this offset from the physical surface. Furthermore, the High Roughness approach requires a fully resolved boundary layer with y^+ values on the order of unity. A posterior inspection of this parameter has been therefore conducted for the highest Reynolds number test point.

The solver controls and convergence settings have been configured to achieve a steady-state solution suitable for meaningful comparison with experimental data. A high resolution scheme for turbulence numerics has been adopted, combined with automatic timescale control using the conservative length-scale option to prevent unphysical divergence [42]. The minimum RMS residuals threshold has been set to 1×10^{-5}. Additional convergence criteria have been introduced to account for potential transient-like behaviour. Specifically, both the outlet pressure and the maximum temperature at the solder–channel interface were required to exhibit an RMS variation below 1×10^{-5} over 25 iterations for the solver to achieve convergence.
The static inlet temperature, total inlet pressure, and outlet mass flow rate boundary conditions have been prescribed according to the nominal experimental values reported in Table 4.1. Additionally, convective heat transfer boundary conditions have been assumed at insulation outer walls considering a uniform heat transfer coefficient and temperature of surrounding air of respectively 10 $\mathrm{Wm^{-2}\,K^{-1}}$ and 293 K. Concerning the boundary heating conditions, a prescribed wall heat flux was imposed along the cartridge housing walls based on the percentage input power supplied during the tests. Naturally, this value exhibited a slight variability relative to the commanded input during experimental trial. Moreover, numerical model simplifications and assumptions inevitably condition the effective heat flux transmitted to the test article with respect to experimental conditions. To account for these aspects, a parametric study was conducted to achieve a sufficiently close match between the numerical and experimental outlet temperatures for each test point. The heat flux boundary condition was considered acceptable when the numerical outlet temperature, evaluated as the mean value of the three temperature rake thermocouples,

matched the experimental value within a tolerance of ±0.5 K. Table 4.3 compares the experimental and numerical outlet temperature values after the tuning procedure.

Test point ID	$T_{out,exp}$ [K]	$T_{out,num}$ [K]
1	634.75	634.28
2	631.47	631.76
3	619.50	619.51
4	598.53	598.98
5	582.62	582.39
6	572.38	572.81

Table 4.3: Comparison between experimental and numerically outlet temperatures after heat flux tuning.

5 | Results and discussion

The present chapter illustrates the most relevant outcomes of the aforementioned research activities. For clarity, the experimental and numerical results are first presented in Section 5.1 and Section 5.2, respectively, and subsequently discussed in Section 5.3.

5.1 Experimental outcomes

5.1.1 Trial 1

With regard to the experimental assumptions validation, the frictional pressure drop across the inlet nozzle and diffuser, relative to the upstream pressure p_{us}, was evaluated to verify whether compressibility effects can be neglected in the estimation of Δp_f. Table 5.1 shows that the maximum frictional pressure drop across these elements does not exceed 4.41% for the nozzle and 2.61% for the diffuser, remaining well below the 10% threshold indicated in the Crane manual [39].

Test point ID	**Nozzle** $\frac{\Delta p_f}{p_{us}}$	**Diffuser** $\frac{\Delta p_f}{p_{us}}$
1	0.0414	0.0261
2	0.0397	0.0243
3	0.0376	0.0220
4	0.0364	0.0208
5	0.0360	0.0203
6	0.0356	0.0198

Table 5.1: Friction loss ratios $\frac{\Delta p_f}{p_{us}}$ evaluated across the nozzle and diffuser for each test point.

A preliminary comparison of the heat transfer coefficients across all test points was per-

formed to provide an overall view of the heat transfer trend with increasing mass flow rate and, consequently, Reynolds number. Figure 5.1 presents the heat transfer coefficients at TWH and TEH stations together with their absolute associated uncertainties.

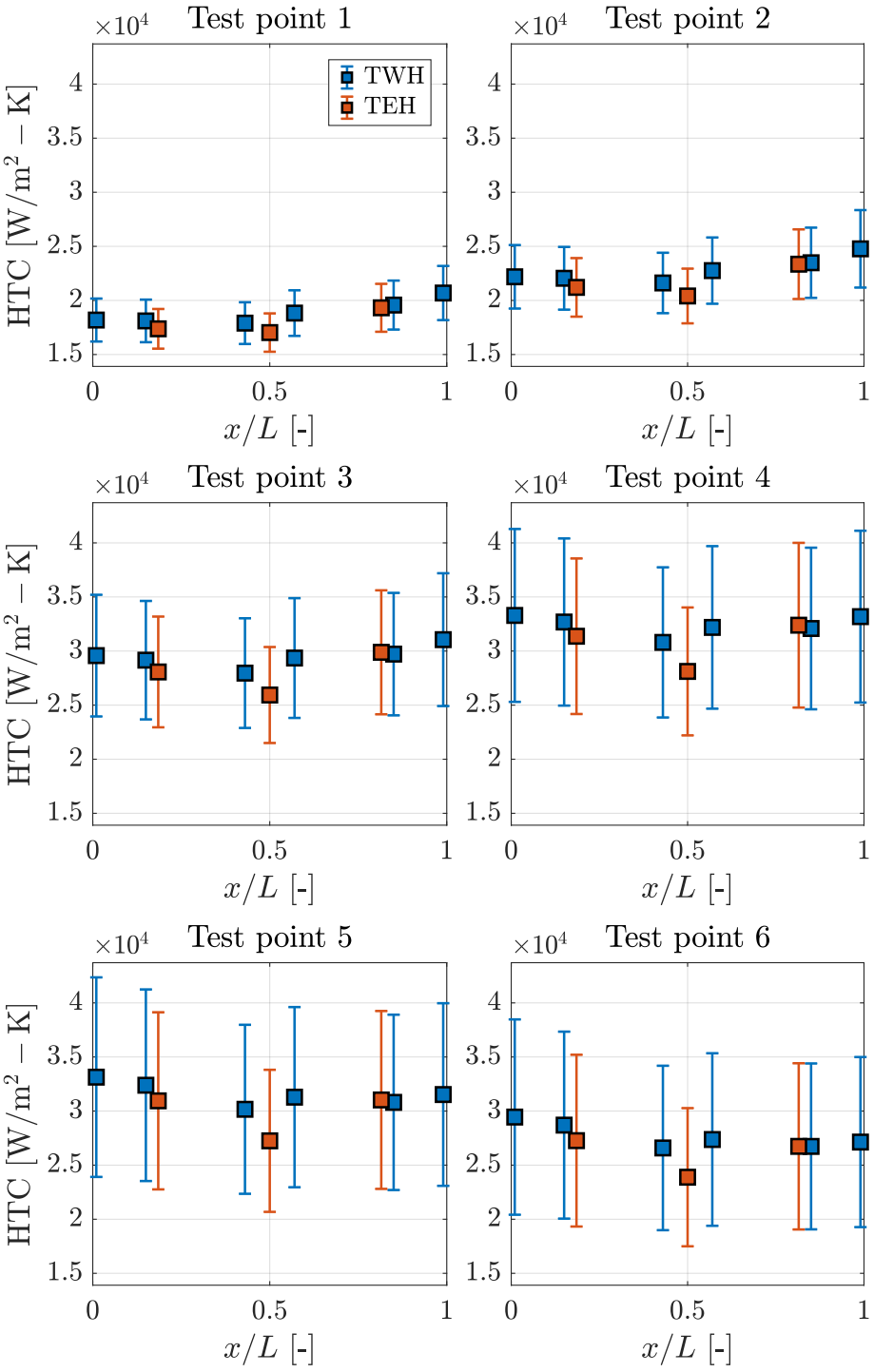

Figure 5.1: Heat transfer coefficient comparison between test points.

Dimensionless heat transfer parameters such as Stanton and Nusselt numbers were compared with typical correlations available in the literature. Most of these relations are based on semi-empirical approaches derived from experimental data for smooth channels under fully developed flow conditions. Similarly, Eq. (2.5) validity, which accounts for roughness effects, holds for hydrodynamically fully established flows. Consequently, only those stations allowing for a meaningful comparison need to be designated. In this context, different rules of thumb and approaches can be used to estimate the channel entrance length L_{entr}. In their heat transfer investigation of rough pipes, for example, Owen and Thomson [43] adopted a typical formulation for boundary layer development expressed as $\frac{L_{entr}}{D_h} = 1.359\, Re^{0.25}$. Considering the present study critical conditions, corresponding to the highest Reynolds number test point, this expression yields an entrance-length to hydraulic-diameter ratio of approximately 38, approximately beyond half of the channel length. On the other hand, outlet effects may also influence the heat transfer behaviour. Consequently, the most downstream temperature probing station of the channel was excluded from the following assessments. For clarity in the graphs presented hereafter, and to maintain a conservative margin with respect to the estimated entrance length, data from the TWH306, TEH307, and TWH308 stations were selected as reference for comparison.

Figure 5.2 compares the experimentally determined Stanton numbers with those predicted by Eq. (2.5). The Darcy friction factor f was evaluated according to the definition provided in Eq. (5.1) from the Crane manual [39], which accounts for compressibility effects by averaging the fluid density and velocity at the stations where the pressure drop occurs.

$$f_{Darcy} = \frac{2D_h}{\left(\frac{\rho_{306}+\rho_{308}}{2}\right)\left(\frac{u_{306}+u_{308}}{2}\right)^2}\left(\frac{p_{306}-p_{308}}{x_{308}-x_{306}}\right) \tag{5.1}$$

where subscripts 306 and 308 denote the values at the corresponding measurement stations. In this case, the k_f parameter was kept fixed at 5.19, yielding a relatively good fit across all test points. Additionally, an optimization procedure has been implemented to determine the k_f value providing the best match between experimental and predicted Stanton numbers. To this end, an unconstrained nonlinear solver was employed to minimize the least-squares error between the experimental and relation-predicted dataset. Specifically, the `lsqcurvefit` function MATLAB was used, with relative and absolute tolerances set to 1×10^{-6}. This procedure yielded an optimal value of $k_f = 4.88$.

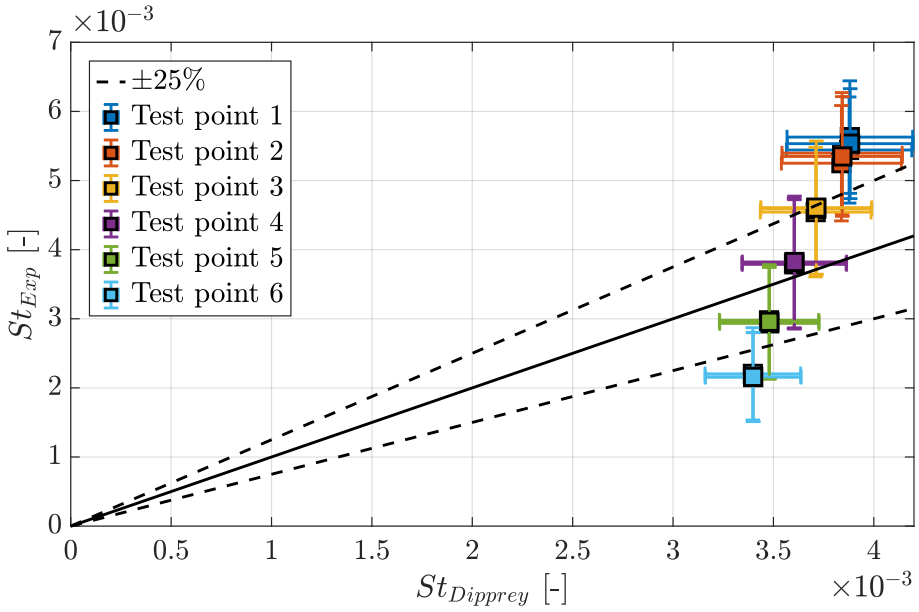

Figure 5.2: Comparison between experimental Stanton number and relation Eq. (2.5) for fully developed stations TWH306, TEH307, TWH308.

Figure 5.3, instead, compares experimental Nusselt numbers with semi-empirical correlations. In particular, Gnielinski and Dittus–Boelter formulations, reported in Eqs. (5.2) and (5.3), were selected.

$$Nu_{Gnielinski} = \frac{\left(\frac{f_{\text{smooth}}}{8}\right)(Re - 1000)\,Pr}{1 + 12.7\sqrt{\frac{f_{\text{smooth}}}{8}}\,(Pr^{2/3} - 1)} \tag{5.2}$$

$$Nu_{DB} = 0.023\,Re^{0.8}Pr^{0.4} \tag{5.3}$$

Here, Pr is the gas Prandtl number, while f_{smooth} is the friction factor corresponding to a smooth surface, evaluated using the formulation proposed by Petukhov [44], shown in Eq. (5.4).

$$f_{\text{smooth}} = (1.82\log_{10}(Re) - 1.64)^{-2} \tag{5.4}$$

It should be noted that these correlations require appropriate correction factors when significant variations of fluid properties occur between the core flow and the wall [44, 45]. Such corrections are often expressed as $(Pr_b/Pr_s)^n$ for the Gnielinski correlation

and $(T_b/T_s)^m$ for the Dittus–Boelter correlation, where the subscripts b and s refer to bulk and surface properties, respectively, and the coefficients m and n depend on the fluid type. These property variations typically arise near transcritical transitions and have limited influence on gases or supercritical fluids. Moreover, considering the low heat input employed during the first and third trials, together with the preheating conditions, the temperature difference between bulk and wall regions has proved to have a minimal impact on heat transfer for the investigated cases.

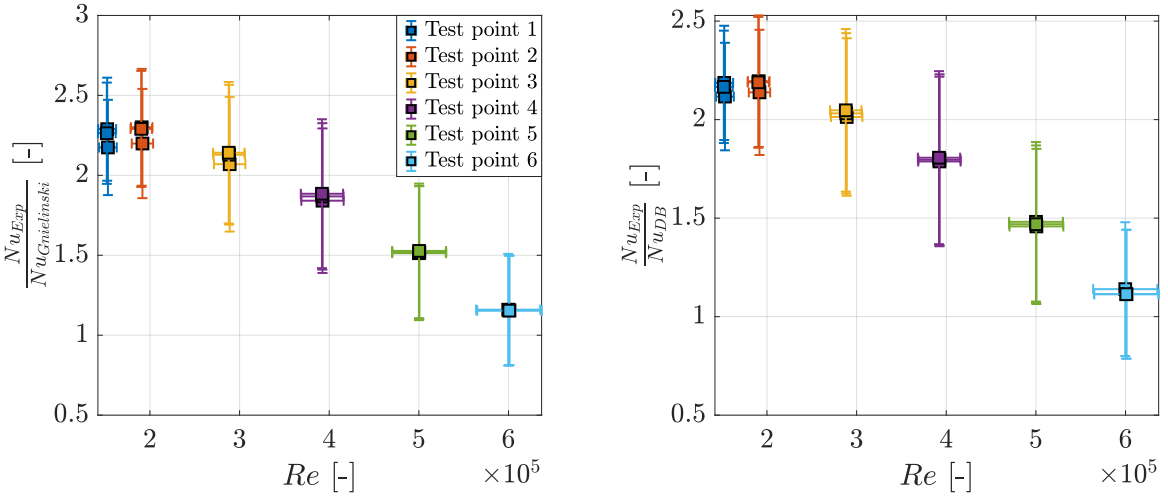

(a) Comparison with Gnielinski Nusselt number.

(b) Comparison with Ditus-Boelter Nusselt number.

Figure 5.3: Comparison between Experimental Nusselt number and semi-empirical relations for smooth channels.

5.1.2 Trial 2

A review of the operating conditions and real-time thermal cracking sensor readings is presented hereafter. Figure 5.4 shows the trends of the TWH sensor readings during the high-temperature methane trial. An enlargement of TWH304 and TWH306 readings is offered to illustrate their close alignment. Long-term temperature fluctuations are observable in the graph due to manual tuning of the supplied power. As previously mentioned, this procedure aimed to prevent the cartridges from exceeding their maximum operating temperature while ensuring the highest achievable channel temperature. A stable power setting was reached approximately 20 minutes after the start of the trial.

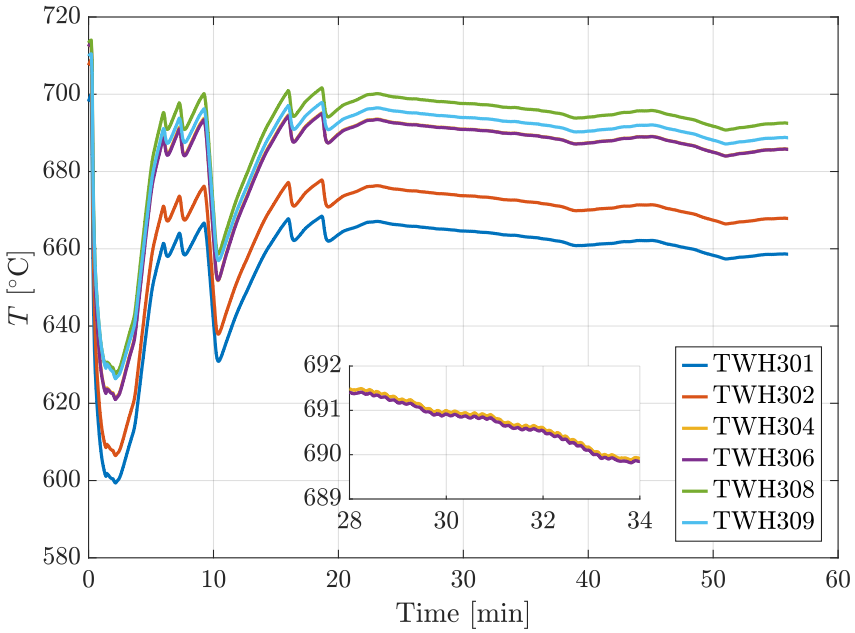

Figure 5.4: TWH sensors readings over test time.

Figures 5.5 and 5.6 illustrate the temperature and pressure readings acquired by the sensors installed along the bypass line. The line embedded thermocouple is particularly sensitive to temperature variations and allows fluid property changes attributable to temperature effects to be distinguished from those associated with alterations in the effluent gas composition.

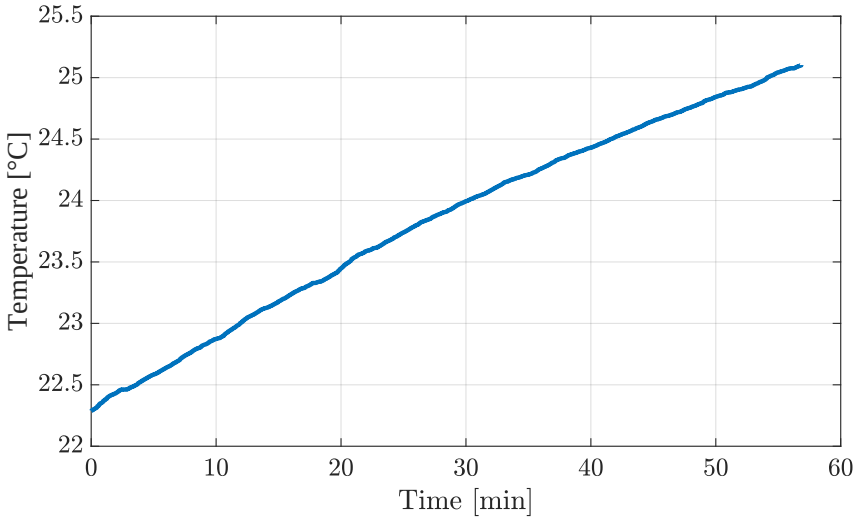

Figure 5.5: Temperature level at SoS sensor probing point.

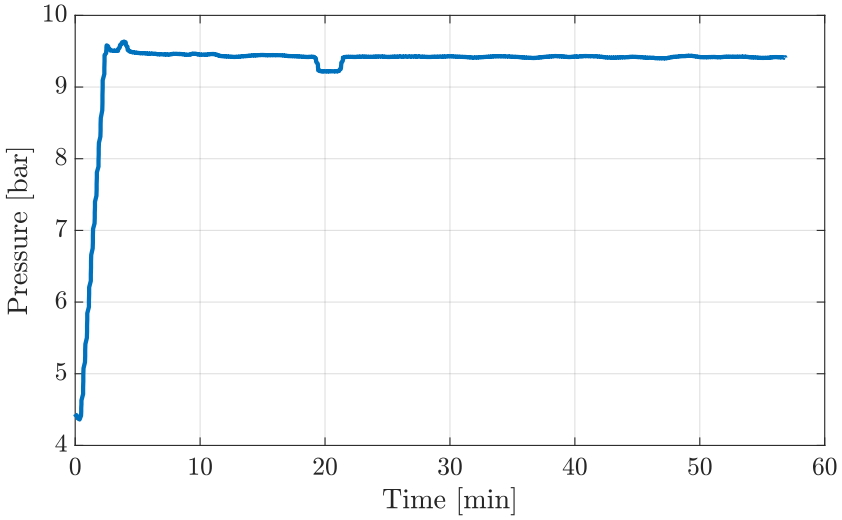

Figure 5.6: Pressure level at SoS sensor probing point.

Figure 5.7 shows the speed-of-sound sensor readings for three relevant measurement modes, denominated 102, 103, and 104. These modes correspond to different thresholds of the returned signal intensity used for the time-of-flight measurement. As the signal threshold increases, the measured time of flight also increases due to the additional delay in triggering the receiver detector. Post-processing of the three measurement modes allows discrimination between variations attributable to sensor noise and recurring changes indicative of an actual variation in the speed of sound due to gas properties alteration.

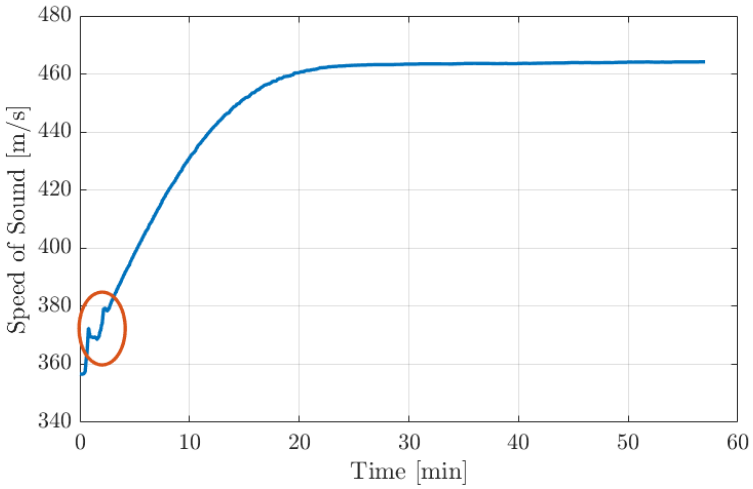

(a) 102 probing mode.

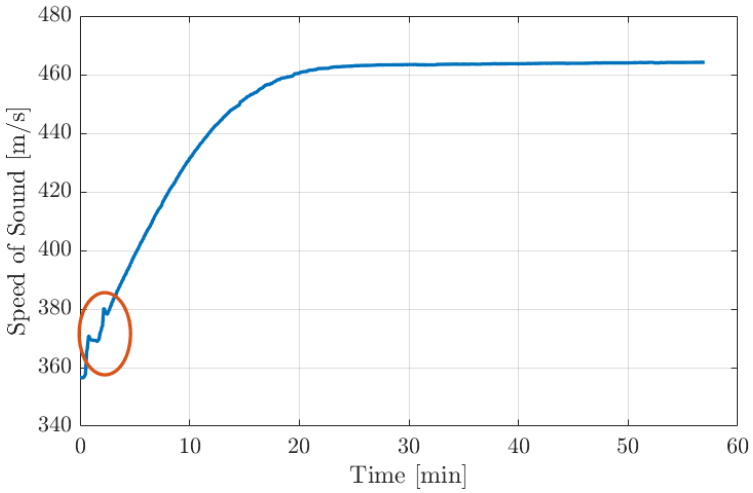

(b) 103 probing mode.

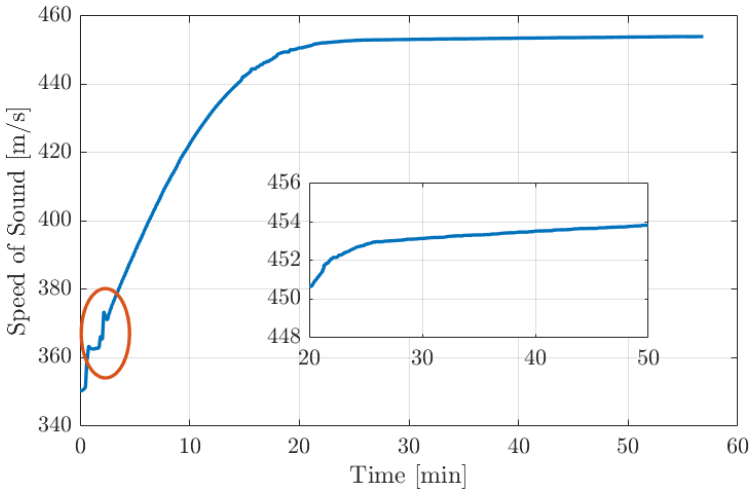

(c) 104 probing mode.

Figure 5.7: SoS sensor readings.

5.1.3 Comparison between Trial 1 and Trial 3

An immediate effect of heat transfer degradation due to coking can be observed through the overall heat pick-up across the test section. As previously mentioned, the temperature rake installed at the channel outlet allows the fluid temperature stratification to be accounted for, thus providing a meaningful basis for comparison of the energetic increment. Figure 5.8 shows the ratio of absorbed heat rate between the first and third trials for all test points.

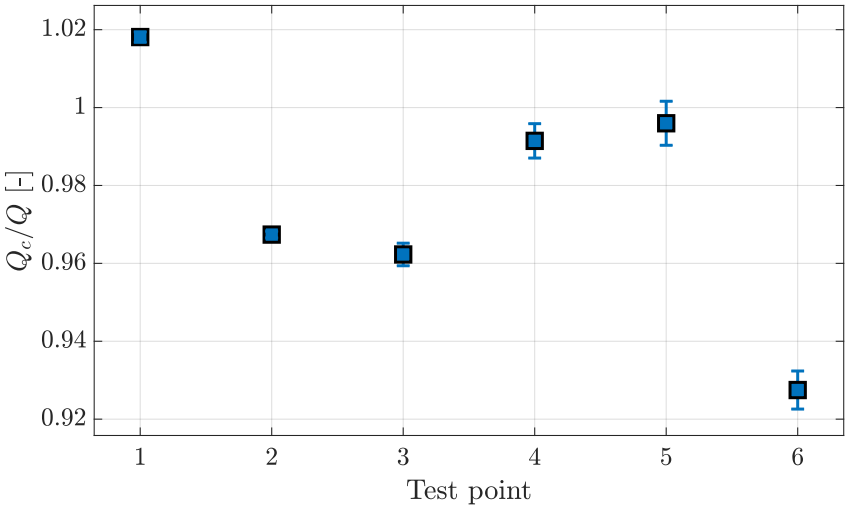

Figure 5.8: Heat pick-up ratio for all test point.

The eventual coking that occurred during the pyrolysis trial can also be assessed through a direct comparison of the heat transfer coefficients and, consequently, of the adimensional parameters describing the heat transfer along the temperature probing stations. Nonetheless, in light of the intrinsic variability associated with the experimental instrumentation, achieving identical test conditions is not feasible with the current set-up. Such variability inevitably affects the inflow temperature and pressure, as well as the mass flow rate. In view of these differences, a normalization factor must be applied to enable a meaningful comparison between the outcomes of the first and third trials. To this end, the channel inlet temperature immediately downstream of the inlet nozzle was selected as the reference parameter. This quantity is derived using compressible-flow assumptions and therefore indirectly incorporates the combined effects of all variable inflow parameters. For identical channel surface conditions, higher inlet temperatures correspond to lower Nusselt numbers, according to the definition provided in Eq. (2.17). Accordingly, the Nusselt number ratio is presented using the definition given in Eq. (5.5).

$$\frac{Nu_c}{Nu}\frac{T_{in}}{T_{in,c}} \tag{5.5}$$

where the subscript c denotes the parameters associated with the potentially coked-channel run. Figure 5.9 shows the experimental Nusselt number ratio between the third and first trials for all thermocouple stations, normalized according to Eq. (5.5).

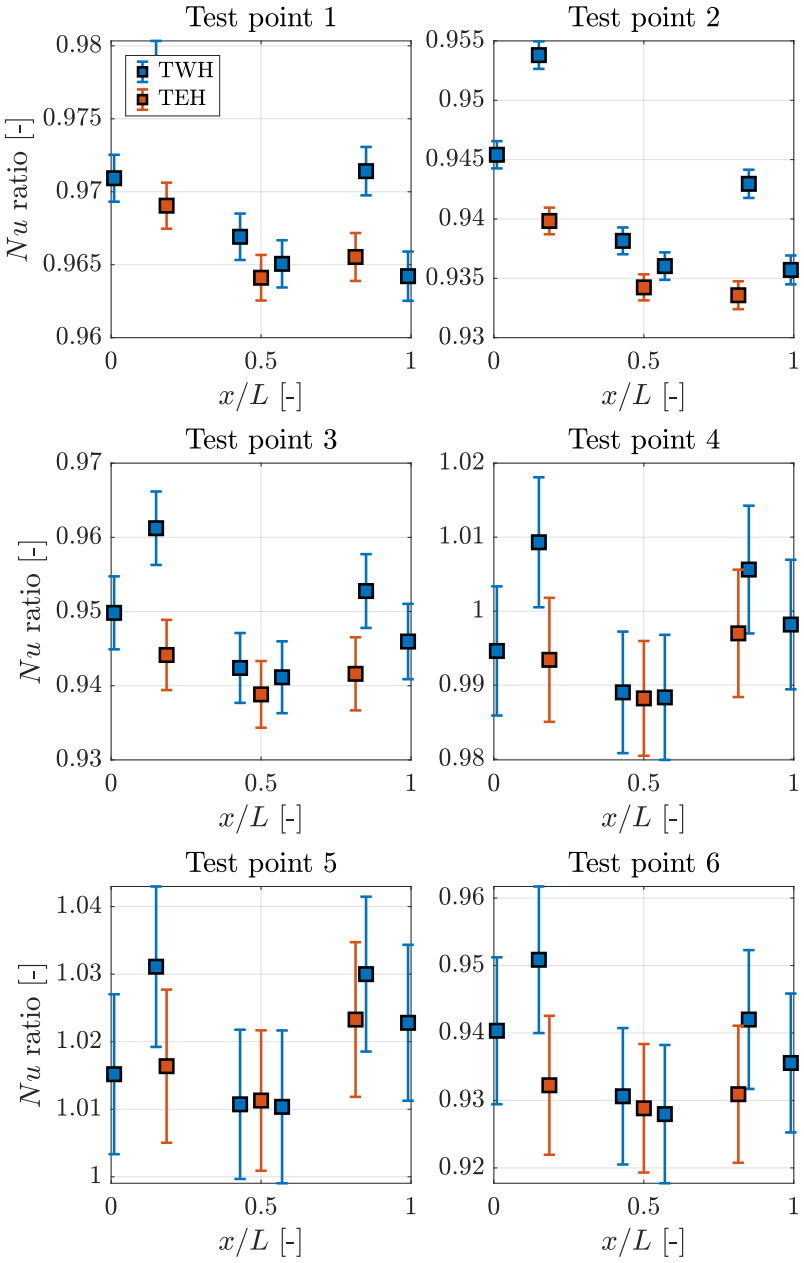

Figure 5.9: Normalized Nusselt number ratio for all test points.

It should be noted that the uncertainty levels reported in Figures 5.8 and 5.9 refer only

to the random errors observed during the two trials. The reader is referred to Appendix A for further details on the adopted uncertainty analysis. This choice is considered appropriate since both trials were conducted using the same experimental configuration, instrumentation, and coolant. Consequently, despite the slight differences in test-point operating conditions, systematic errors are expected to affect the results in a very similar manner and can therefore be reasonably neglected in the present comparison.

5.2 Numerical outcomes

Relevant outcomes of the numerical analysis are presented hereafter to assess the effectiveness of the numerical methodology in predicting roughness effects on fluid behaviour and heat transfer characteristics through the GKN1 thermal correction model, as well as to evaluate the accuracy of the experimental modelling in predicting fluid pressure and temperature trends.

Firstly, mesh wall resolution is assessed through the y^+ parameter in Figure 5.10 for the highest mass flow rate test point. The y^+ values do not significantly deviate from unity along the channel length, thus falling within the typical applicability range of the HR approach.

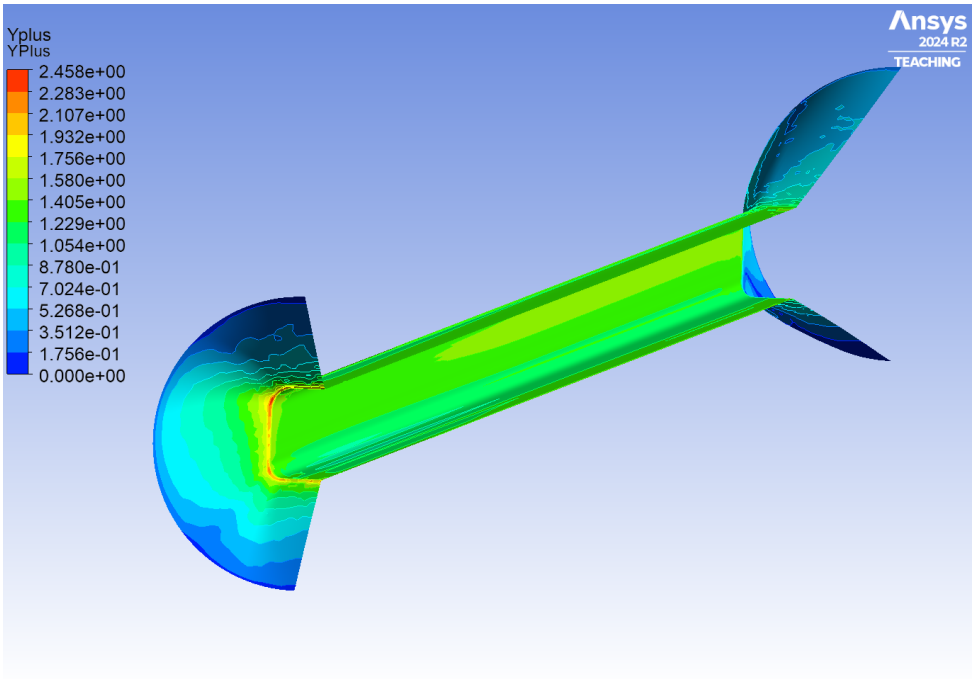

Figure 5.10: y^+ distribution for test point 6.

The roughness Reynolds number k_s^+ for test point 1 was extracted to verify the appli-

cability of Eq. (2.5) and is presented in Figure 5.11. As shown, the k_s^+ values along the entire channel length remain well above the typical threshold for the fully rough regime for sand-grain-type roughness, which is commonly taken to be approximately $k^+_{\text{Rough}} \approx 70$ as also expressed in the g_{2pp} function in GKN1 correction model. As the fluid velocity increases, wall shear stress also raises, thereby incrementing the shear velocity. Regarding the influence of kinematic viscosity on the roughness Reynolds number, this does not vary significantly along the channel length, as can also be inferred from Figure 5.11. Lower k_s^+ values occur in proximity to the heated channel base, where higher temperatures increase the kinematic viscosity in the near-wall region.

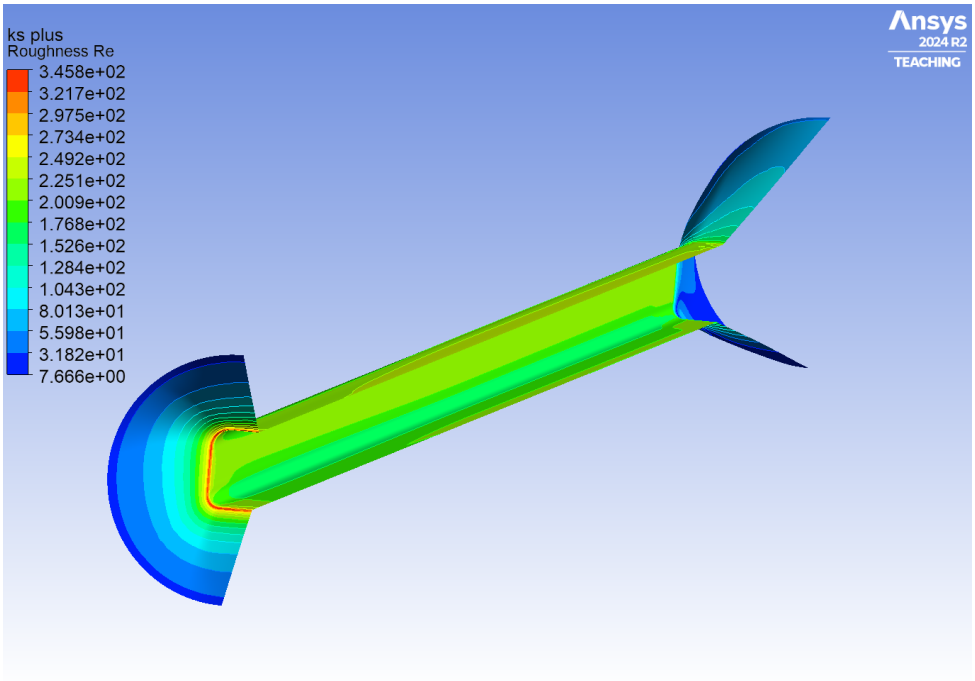

Figure 5.11: Roughness Reynolds number distribution along the channel for test point 1.

Additionally, the validity of the adiabatic-flow assumption adopted in the experimental model for the inlet nozzle and outlet diffuser is assessed. The wall heat flux within the channel domain is plotted in Figure 5.12 for test point 1. As can be inferred, the connecting elements still exchange a non-negligible amount of heat with the gas. However, moving away from the heated section, the heat transfer trend reverses along these regions, which are characterized by an increased contact surface area. This indicates that, as the fluid departs from the channel inlet and outlet, it is no longer heated but cooled down. Such dual behaviour during flow transition may partially compensate for the error introduced by the fully adiabatic-flow assumption adopted in the experimental model. This characteristic is observed for all analysed mass flow rate cases, with only minor

variations in the magnitude of heat exchange.

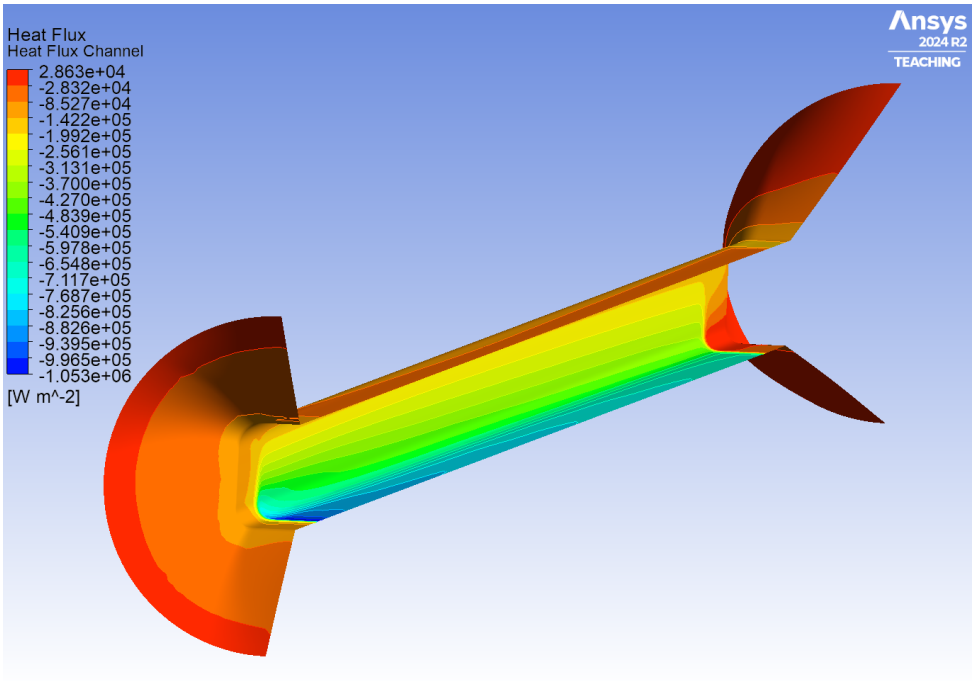

Figure 5.12: Wall heat flux with respect to channel domain for test point 1.

The comparison between experimental and numerical results was performed by extracting solid-domain variables at prescribed locations corresponding to the positions of the temperature sensors. In addition, fluid bulk parameters were sampled along the channel centreline. These locations are illustrated in Figure 5.13.

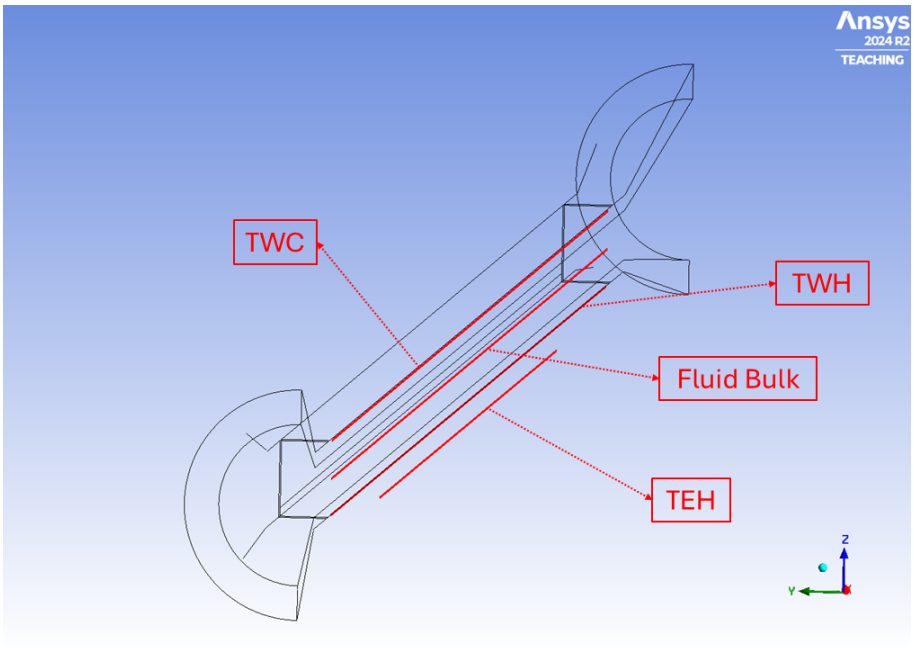

Figure 5.13: Reference locations for data comparison.

Significant graphs comparing numerical and experimental conditions along the channel length are presented hereafter in Figures 5.14 to 5.18. Additionally, Figure 5.19 shows the numerically predicted HTC according to the same definition provided in Eq. (2.17).

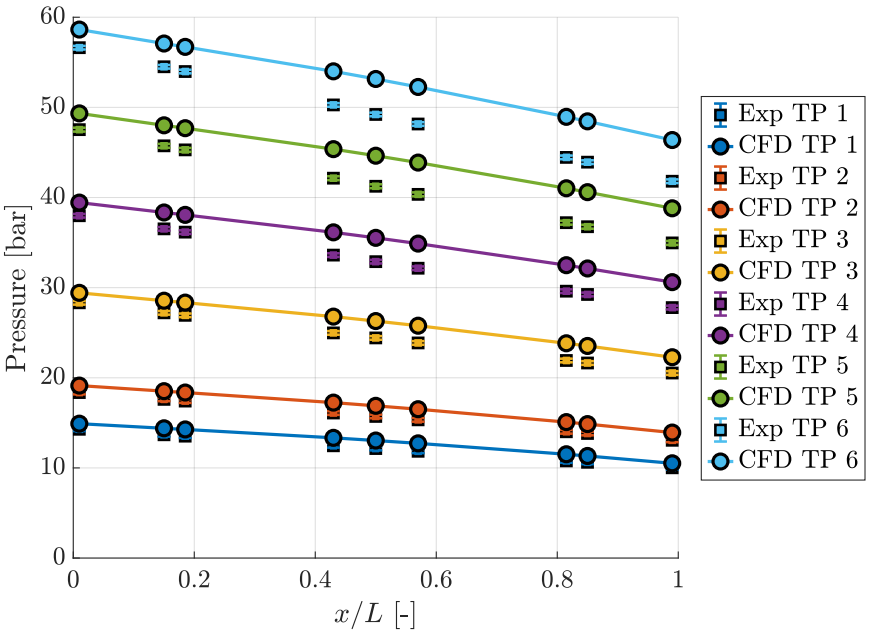

Figure 5.14: Pressures comparison at TWH and TEH stations along the channel length.

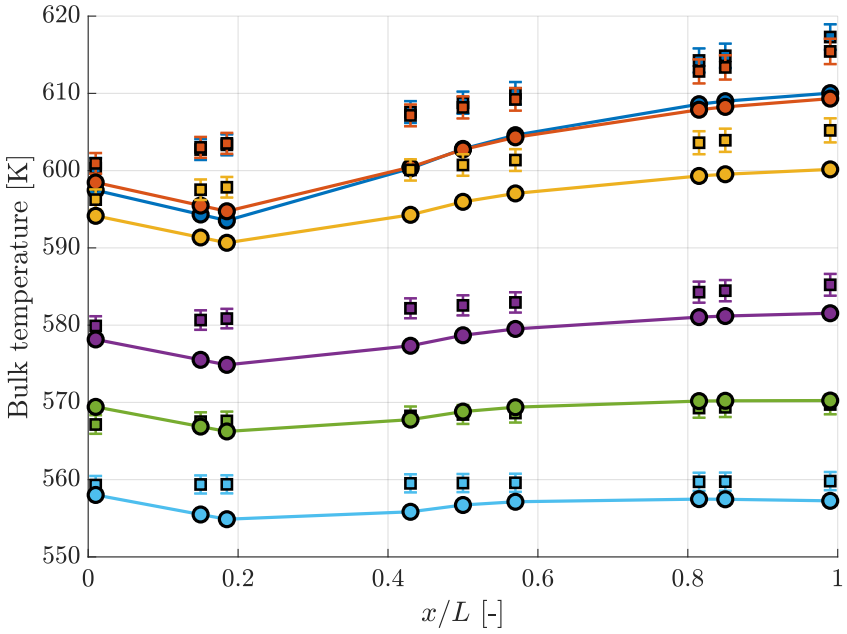

Figure 5.15: Bulk temperatures comparison at TWH and TEH stations along the channel length.

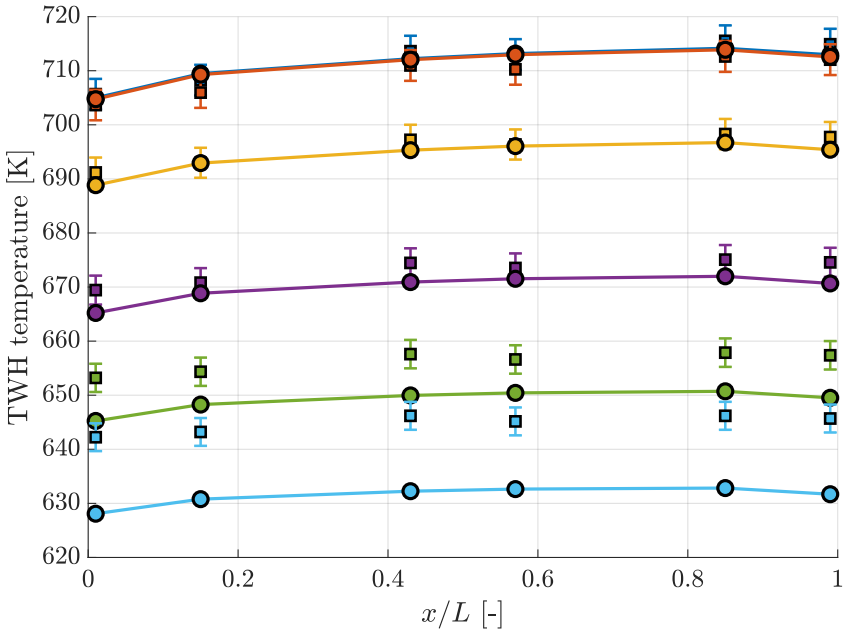

Figure 5.16: Temperatures comparison at TWH probing points.

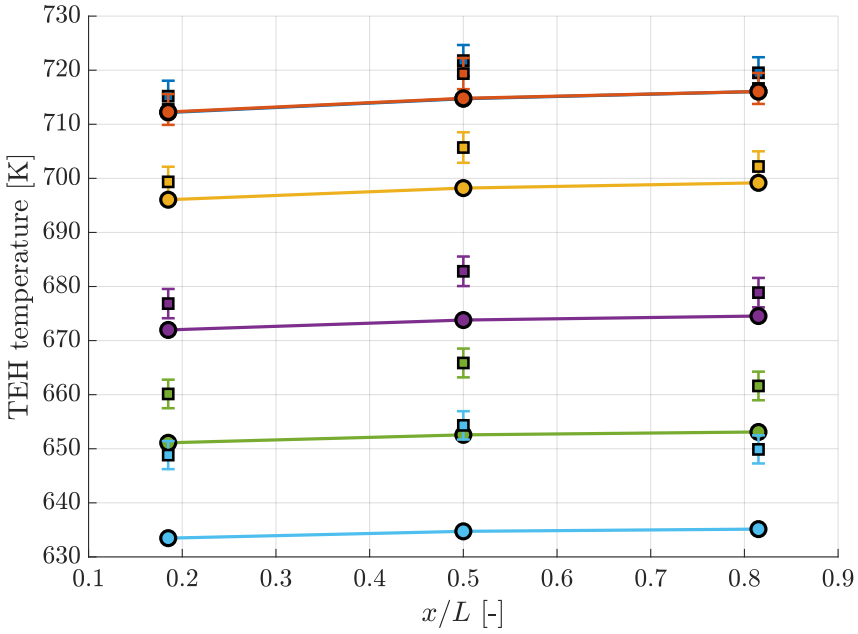

Figure 5.17: Temperature levels comparison at TEH probing points.

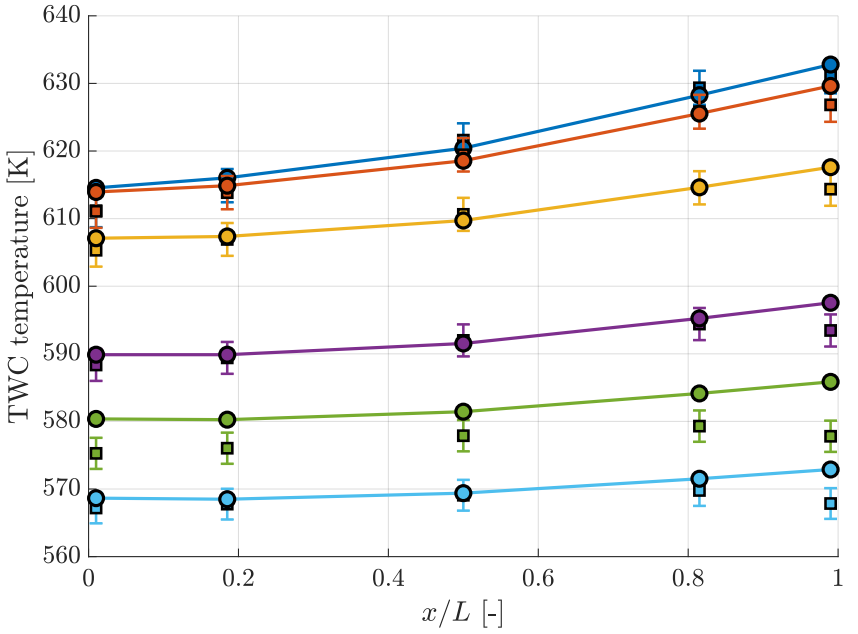

Figure 5.18: Temperature level comparison at TWC probing points.

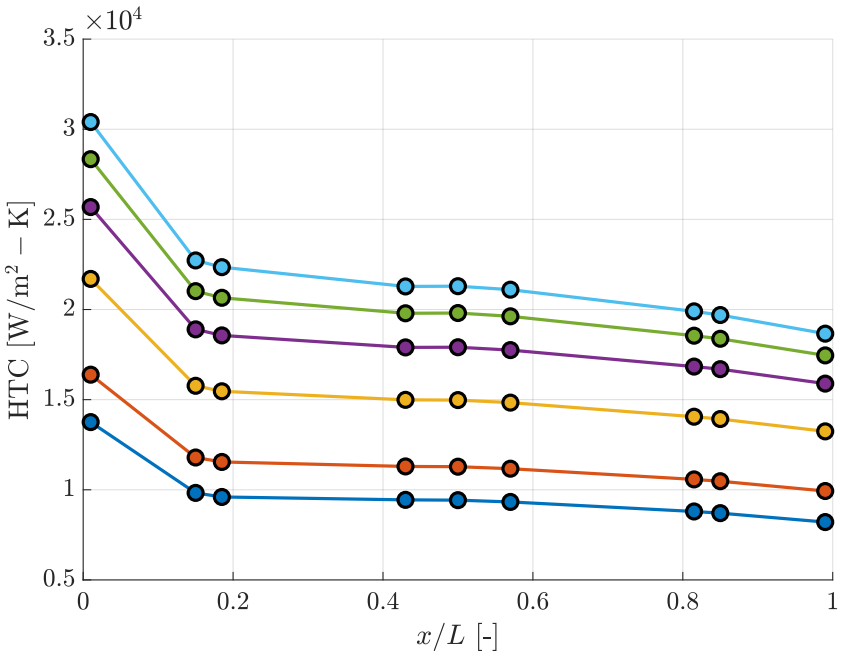

Figure 5.19: Numerically predicted HTCs at TWH and TEH stations for the analysed test points.

5.3 Discussion

In light of the results presented in the previous sections, several remarks are provided to facilitate data interpretation. First, a note on the uncertainty levels associated with the experimental data set. As can be observed in Figure 5.1, the HTC absolute uncertainty increases significantly, reaching values up to approximately 29%. This marked increase is associated with the experimental data-processing procedure and, specifically, with the energy balance used to determine the heat transferred to the fluid. As the temperature difference between the inlet and outlet rake stations decreases, the uncertainty is amplified by the subtraction of enthalpy terms in Eq. (2.18). The uncertainty in the enthalpy values is strongly dependent on thermocouple accuracy, which remains of the same order of magnitude at both inlet and outlet temperatures for all analysed cases. When the enthalpy difference across the test section becomes comparable to its uncertainty level, the resulting heat-rate estimate exhibits large uncertainty, which subsequently propagates to the HTC evaluation.

Despite the high uncertainty levels, several observations can be made regarding the HTC trends shown in Figure 5.1. Entrance effects would normally lead to enhanced heat transfer near the first channel stations. However, this behaviour cannot be captured by the current experimental model because the heat rate is assumed constant and equal to

the value obtained from the overall energy balance. As a term of comparison, the reader is referred to numerically predicted HTCs in Figure 5.19. In this graph, the represented HTC values consider the effective heat transfer occurring at the wetted base surface as well as the corresponding surface temperatures. Both these quantities are probed on the line located at the same symmetry plane of the other reference locations in Figure 5.13.

Considering the effective heat rate showed in Figure 5.12, it is evident that the cooling effect provided by the fluid, in terms of absorbed heat flux, is more pronounced in the channel entrance region. It should be noted that these effective values remain lower than the global heat flux used in the experimental HTC calculations. For example, for test point 1 the heat flux obtained from the energy balance is approximately 1.1 MW, whereas numerical simulations indicate values ranging from about 1.0 MW to 0.66 MW along the channel base inner surface at the corresponding TWH stations. This also indicates that the side and top walls contribute significantly to the overall fluid temperature increment. Consequently, the experimental Stanton numbers reported in Figure 5.2 are likely shifted upward relative to their actual values. This consideration motivated the adoption of a slightly higher k_f value in the numerical simulations compared with that obtained from the optimization procedure, in order to partially compensate for the experimental overestimation of the Stanton number. With regard to Figure 5.3, minor qualitative conclusions can be drawn, since both the Gnielinski and Dittus–Boelter correlations were semi-empirically derived from smooth-channel data sets. Nevertheless, the presence of roughness elements clearly enhances heat transfer with respect to equivalent smooth surfaces. Increased turbulence levels near the wall intensify momentum-driven energy transport, thereby promoting higher heat transfer rates.

Referring to the pressure-drop comparison between numerical and experimental values, the experimental results closely align with the CFD predictions at low mass flow rates, highlighting the reliability of the HR model. It should be recalled that Raj et al. [38] derived the corresponding $k_s = 39$ μm using a hydraulic diameter obtained from optical microscopy measurements, yielding a relative roughness of approximately 0.0195. If the nominal channel hydraulic diameter is considered, this relative roughness would instead correspond to $k_s/D_h = 0.0134$. This raises the question of how the equivalent sand-grain roughness of $k_s = 57$ μm adopted in the present investigation can still provide general agreement with experiments, given that the relative roughness is effectively increased with respect to the value derived by Raj et al. [38]. A possible explanation is provided by Östlund [15], who noted that the HR roughness model, originally developed for external flows, may require a relative roughness approximately twice that retrieved through the Moody diagram in order to reproduce the same experimentally observed friction factor.

In the work of Raj et al. [38], in fact, the Darcy friction factor was used to derive the experimental k_s value of 39 μm. Consequently, the relative roughness adopted in the present study, referred to the nominal hydraulic diameter, results approximately 1.5 time higher than the one that can be derived through previous investigations. Additionally, Raj et al. [38] likely employed a different numerical approach to model roughness effects on pressure drop, as they reported the use of a wall-function-based turbulence model that does not require resolution of the near-wall region. This would also explain why their numerical assessment did not required an increased relative roughness with respect to the one observed experimentally.

Despite these observations, it remains unclear why the experimental pressure drops at higher mass flow rates gradually diverge from the numerical predictions, particularly in the most downstream sections of the channel. Two main hypotheses were therefore considered. The first hypothesis lies in the aforementioned observations about the relative roughness employed in the numerical model. In spite of a general agreement for lower investigated Reynolds number, such a value still presents an offset with respect to the findings by Östlund [15]. Therefore, it can be reasonably assumed that increasing the equivalent surface roughness, yielding a relative roughness value closer to 2 times the one observed in the Moody diagram, would worsen the fit for lower mass flow rates but enhance the overall match for higher Reynolds number. An alternative explanation may be related to the flow behaviour during the transition from the channel to the outlet diffuser. To clarify this aspect, the reader is referred to Table 5.2, which reports the outlet pressure measured at the P104 pressure tap.

Test point ID	$p_{out,exp}$ [bar]	$p_{out,num}$ [bar]
1	11.53	11.53
2	14.85	15.16
3	22.98	24.07
4	30.86	32.90
5	38.68	41.61
6	46.13	49.72

Table 5.2: Experimental and numerical outlet pressures for each test point.

From the aforementioned table, it can be observed that the numerical pressure drop is slightly underestimated compared with the experimental values. In this regard, Pettersson

[2] highlighted the potential risk of flow separation resulting from the combined effects of thermal stratification in the region closest to the heated base and the particularly strong adverse pressure gradients developing within the outlet diffuser. An inspection of streamlines from the rough-channel numerical simulation indicates that flow separation does not occur within the outlet diffuser. This behaviour may be attributed to the enhanced turbulence levels induced by surface roughness, which promote earlier transition of the boundary layer to turbulence, making it less prone to separation than a laminar boundary layer. To further clarify this potential mechanism, a smooth-channel simulation was performed using the same boundary conditions as test point 6, representing the most critical case with respect to pressure-drop variation across the diffuser. Figure 5.20 compares the outlet diffuser streamlines for the smooth and rough configurations.

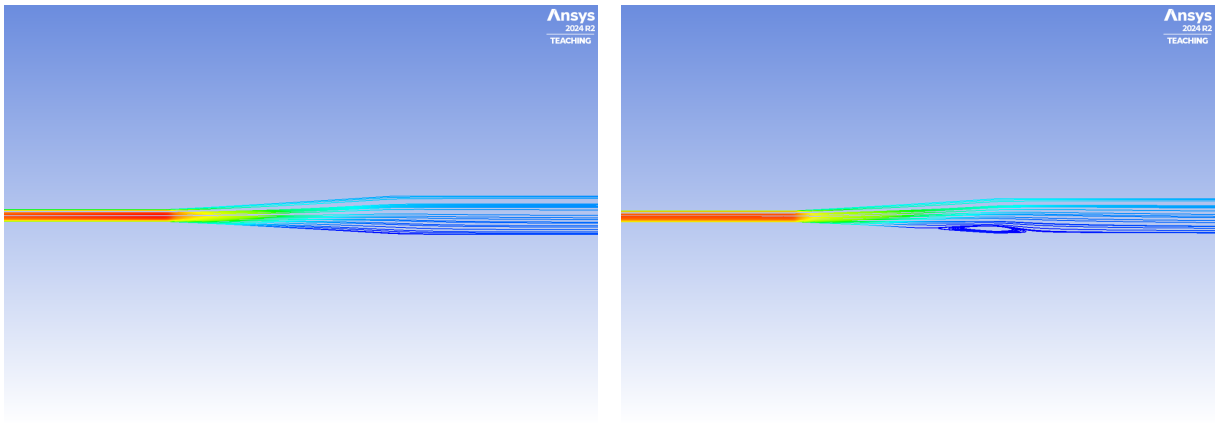

(a) Rough channel case. (b) Smooth channel case.

Figure 5.20: Outlet diffuser streamlines comparison for test point 6 boundary conditions.

It is evident that a recirculation zone develops near the base wall of the outlet diffuser in the smooth-channel configuration. The SST model is generally expected to provide improved predictions of flow separation. However, RANS models often struggle to accurately predict both the onset and the extent of separation [42]. Moreover, no specific information is available regarding the treatment of flow separation when the Ansys CFX HR model is coupled with the SST turbulence formulation. Likewise, Aupoix and Spalart [17], in developing the roughness correction terms included in Ansys solver, did not address the model capability to predict wall separation. Therefore, it is possible that flow separation actually occurs within the outlet diffuser and is not captured by the numerical model. Conversely, the experimental model does not account for such potential separation, since the pressure variation across the diffuser is estimated using an adiabatic-flow assumption combined with frictional pressure losses. As a result, the pressure drop through the diffuser may be underestimated. Such a scenario presents significant challenges for both

numerical and experimental analyses within the MERiT facility, owing to the inherently three-dimensional and asymmetric nature of flow separation, whose impact on pressure losses is particularly difficult to quantify.

With regard to the fluid temperature variation along the channel, Figure 5.15 shows that the implemented experimental model provides a sufficiently accurate prediction of the temperature trend, despite neglecting the two-dimensional nature of the flow variables across the channel. It can be observed that the discrepancy between experimental and numerically predicted temperatures increases as the average Reynolds number decreases. This behaviour is likely attributable to enhanced turbulent mixing at higher fluid velocities, which promotes temperature homogenization within each channel cross section. Measuring temperature across the entire fluid cross section, rather than along a single centreline, would capture the temperature gradients developing near the wall region and would therefore yield higher temperature values closer to the one that have been derived experimentally, which instead accounts for outlet temperature stratification by averaging the rake thermocouples readings. Independently of the previous consideration, the largest deviation occurs in the channel entrance region, where the flow is still developing and the bulk temperature exhibits a sharp decrease that cannot be captured by simple linear interpolation.

Referring to the thermocouple readings comparison presented in Figures 5.16 and 5.17, it can be observed that the implemented heat transfer correction model predicts the hot-wall-side temperatures with good accuracy up to the mass flow rate corresponding to test point 4. For test points 5 and 6, however, temperatures are clearly underestimated, with maximum discrepancies reaching 13 K for the TWH locations and 20 K for the TEH locations. Conversely, the offsets observed for the TWC readings remain limited across all analysed mass flow rates. In light of these results, several considerations can be made. Regarding the significant mismatch affecting the TEH values, a sensitivity analysis performed by Ristic [1] on temperature measurements as a function of probe insertion depth provides useful insight. In particular, Ristic [1] showed that TEH thermocouple outputs can vary significantly with their axial insertion depth within the copper block, with deviations comparable to those observed in the present study. This divergence becomes more pronounced as thermal gradients increase, which is consistent with the enhanced heat transfer associated with higher mass flow rates. Nonetheless, a further inspection of the top copper block temperature profile for test point 6, in the vicinity of the channel mid-length section, revealed no significant temperature variations along the top block–solder contact region. Following the same reasoning, these observations would, instead, explain why the differences between numerical and experimental TWC temperatures are less pro-

nounced, owing to the more homogeneous temperature distribution in the upper region of the channel cross section. For clarity, the reader is referred to Figure 5.21. Such probes are then less extensively affected by their positioning uncertainty.

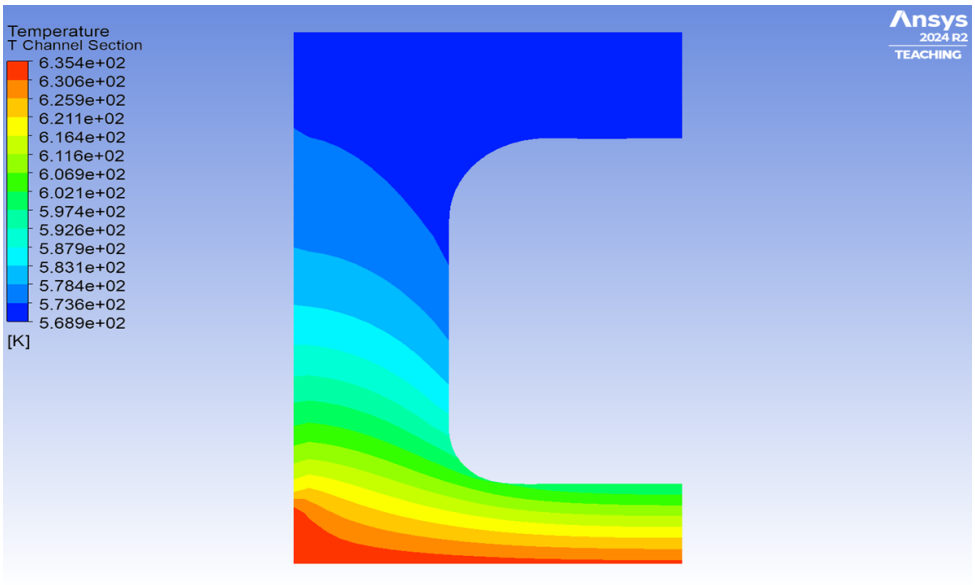

Figure 5.21: Channel section temperature contour at half channel length (not to scale).

On the other hand, the experimental TWH and TEH temperatures are consistently higher than the CFD predictions. These discrepancies are most likely ascribable to additional uncertainties arising in the comparison between experimental and numerical outcomes that has not been considered in Figures 5.16 to 5.18. A post test inspection of test conditions for the first trial, in fact, revealed how, a thermal transient is still occurring in the heated side of the test section, throughout the selected higher mass flow rates probing windows. Figure 5.22 shows the temperature trends of TEH sensors during the whole trial duration. Test points are subsequently achieved from the lowest to the highest mass flow rate. Within these intervals denominated as MF (mass flow) in this graph, the probing window for test point identification is shifted to the most right end of each section in order to refer to the most steady conditions. As can be inferred, TEH temperature trends for the higher mass flow rates test points indicate how proper steady conditions are not completely reached. As a direct consequence, the hot wall side experimental temperatures considered in the previous comparison with CFD results are subject to an increased uncertainty level with respect to low mass flow rate values, which roughly amounts to 1-2% if referring to temperature variations observable within single test point windows in Figure 5.22. The same source of uncertainty affects TWH values but in lesser extent due to the reduced channel thermal inertia, approximately estimated as 0.4-0.8%

of the reported temperature levels in Figure 5.16.
Within this context, it should also be mentioned that the temperature tuning process carried out to match the experimental and numerical outlet temperature additionally impacts the uncertainty level. Percentage variation of power with respect to the nominal level set during trials approximately ranges between 1-2%, compensating for thermal modelling simplifications introduced in the numerical model. In light of these intrinsic conditions characterising the presented framework, it can be concluded that observed TEH and TWH maximum discrepancies between experimental and numerical outcomes fall within the uncertainty levels related to both the adopted experimental and numerical methodology.

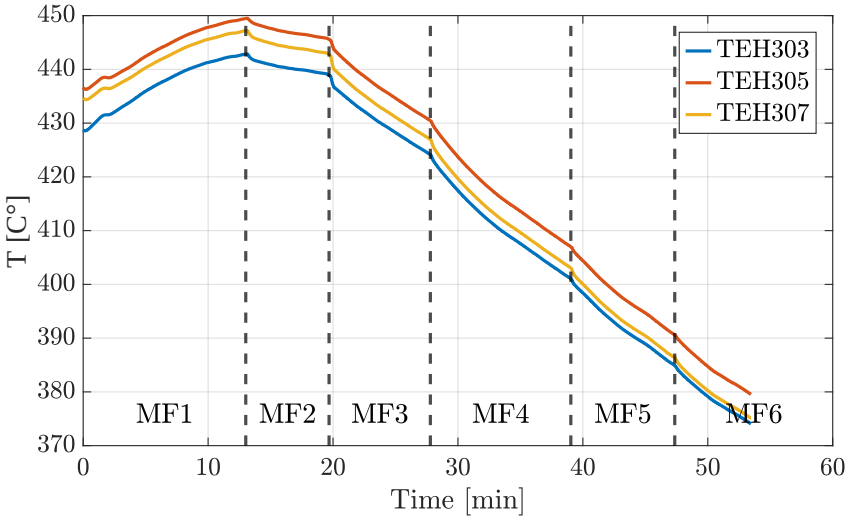

Figure 5.22: TEH temperatures trends over the first trial.

Concerning the real-time assessment of methane thermal cracking, post-processing of the bypass-line sensor outputs revealed no clear evidence of reaction occurrence. Figure 5.7, for instance, shows a substantial increase in the speed of sound that is too abrupt to be attributed to hydrogen enrichment in the effluent gas. This trend is more plausibly explained by nitrogen initially trapped in the bypass line being progressively flushed out through the tapping system. As nitrogen is replaced by methane, a steady increase in sound velocity can be observed in Figure 5.7c. Considering the monotonic temperature trend at the speed-of-sound sensor location shown in Figure 5.5, the slight additional increase is likely associated with the gradual temperature increment of the exhaust flow. Notably, all measuring modes recorded a small peak during the initial test phase that could be consistent with a transient composition change. However, inspection of the pressure trace in Figure 5.6 shows that this peak coincides with the stabilization of the operating

pressure, suggesting an instrumentation-related transient rather than a chemical effect. The absence of definitive evidence of thermal decomposition from real-time measurements in the MERiT facility is not unprecedented. Previous tests conducted with the same instrumentation produced similarly inconclusive results. The primary factors limiting detection capability are the considerable distance between the heated test section outlet and the bypass-line inlet, together with the small fraction of gas diverted from the main flow to the by-pass. As a consequence, any changes in effluent gas composition are delayed and effectively smeared out, preventing clear identification in the sensor signals. For this reason, the present work aimed to explore an alternative approach to assess the occurrence of methane thermal decomposition.

By comparing the outcomes of the first and third trials, several relevant aspects emerge. First, an introductory comment should be made about the followed approach. The evaluation of coking layer effects on heat transfer degradation through fluid heat pick-up represents a substantially indirect method to seize any of these changes. From a purely theoretical point of view, the Nusselt number relates convection and conduction properties of the fluid and does not account for solid interface properties. Nonetheless, the experimental approach adopted for its derivation in the present framework does not isolate completely the contribution of interface temperature, as the HTC is derived from channel surface temperatures. Undoubtedly, a more direct evidence of the coking layer formation could be inferred comparing transient temperature trends of the channel base for the coked and clean case. If an additional thermal resistance is present at the channel-fluid interface, then TWH readings should reasonably respond more slowly to temperature changes. This could represent a future implementation for coking layer assessment within the MERiT operating framework.
On the other hand, the inherently transient nature of the conducted trials may represent an additional source of uncertainty affecting the HTC comparison, which has not been evaluated in the present work. In order to enhance the followed approach reliability the selected probing window for test point identification in the third trial, directly referred to the one considered in the first trial. Specifically, the probing interval for a single test point has been chosen so that the time elapsed between the mass flow rate establishment (denoted by the dashed line in Figure 5.22) pertaining to a single test condition and the relative probing window start is the same for the first and the third trial.

The comparison of the fluid absorbed heat rate shown in Figure 5.8 provides an initial indication of potential heat transfer degradation. Test point 1 ratio indicates an increase in heat uptake, whereas the remaining test points exhibit a generally variable decrease. A post-test inspection of the operating conditions revealed no significant discrepancies

between the two trials, with the exception of test point 5 of the first trial. In this case, the mass flow rate trace showed a sudden oscillatory increase after the target conditions had been reached. Shifting the sampling window to an earlier time interval was not considered reliable, since more unstable temperature conditions may affect the comparison. The resulting transient increase in mass flow rate produced a higher Reynolds number, thereby enhancing convective heat transfer at the channel inner surface. Consequently, the heat-rate ratio for test point 5 in Figure 5.8 is likely biased. The same considerations apply to the interpretation of Figure 5.9. In spite of the heat transfer increment registered for the first test point, the associated local Nusselt numbers result decreased with respect to the first case. Moreover, it can be observed how test point 4 did not present remarkable variations of HTC. As previously mentioned, such an inconsistency may be imputed to the time window selection for test point identification related uncertainty.

Generally, Figure 5.9 indicate a Nusselt number decrement with respect to the clean case, especially when referring to TWH304, TEH305 and TWH308 in proximity of the channel half length. It should be recalled that the adopted experimental methodology assumes a constant heat rate, equal to that absorbed by the fluid across the test section, to thermally propagate the TWH readings. As an inevitable consequence, any increase or decrease in heat flux is uniformly applied to all measurement stations. From a physical standpoint, if coke layers formed on the channel surface during the second trial, the effective local heat flux should depend on the amount of deposited carbon in the immediate vicinity of each station. Inspection of Figure 5.4 suggests that the most probable hot spots for carbon deposition lie between stations TWH304 and TWH309. However, it must be emphasized that the effective temperature at the fluid–solid interface is reasonably lower than that measured at the channel base. Taking as reference the most stable test conditions after 20 minutes the start of the trial and considering the one dimensional heat conduction model employed for HTC data processing, the temperatures at surface level result approximately 130° C lower than the ones measured at TWH baseline. Recalling the findings of Heldens et al. [24], rough Haynes 230 samples exhibited evident coking traces at surface temperatures around 700 °C. Although an accurate estimation of the wetted surface temperature cannot be obtained through the aforementioned approach, as also channel top and side surfaces significantly contribute to the fluid heat transfer, channel-fluid interface temperatures are definitely lower with respect to reaction onset levels observed in the literature. Given the limitations of the current framework, both in terms of methodology and available instrumentation, it cannot be conclusively stated that thermal decomposition occurred during the second trial. A post-test inspection of the channel inner surfaces would provide more definitive evidence and should be addressed in future work.

6 | Conclusions

The present study investigated methane as a coolant for regenerative cooling applications in a Haynes230 additively manufactured minichannel within the MERiT experimental facility. The work combined an experimental data-reduction procedure with a conjugate heat transfer CFD framework developed in Ansys® CFX. Existing experimental and numerical methodologies were refined to account for methane compressibility effects along the test section and for the influence of surface roughness on the established flow field and heat transfer. Heat transfer coefficients were experimentally derived through one-dimensional thermal propagation of embedded temperature measurements along the channel walls, assuming a uniform applied heat flux obtained from a global energy balance across the test section. Fluid bulk temperatures were estimated through linear interpolation of flow variables between the channel entrance and exit. Because direct measurements at the channel boundaries were unavailable, pressure and temperature at these locations were reconstructed assuming adiabatic flow through the connecting elements, accounting for cross-sectional area variations and frictional pressure losses. The numerical model of the test section was further refined by implementing the High Roughness (HR) approach together with the GKN1 thermal correction model based on the Dipprey and Sabersky formulation. Roughness effects were modelled through the equivalent sand-grain roughness approach, building on previous studies that characterised the friction behaviour of the same test article. In light of the experimentally observed heat transfer coefficients, other correction coefficients of the models were assumed. In parallel, alternative strategies for detecting methane thermal decomposition were explored. Heat-transfer degradation due to carbon deposition was investigated by comparing the experimentally retrieved Nusselt number of nominally similar test points achieved across two trials. To this end, an additional high-temperature run was interposed between the previous trials in order to promote methane cracking. During this intermediate trial, real-time detection of decomposition was attempted by monitoring effluent gas properties using thermal conductivity and speed-of-sound sensors.

Comparison between experimental and numerical results showed good agreement in both temperature and pressure fields at the lowest Reynolds numbers. However, with increas-

ing mass flow rate, experimental pressure drops progressively deviated from the predicted values, particularly in the downstream region of the channel. In light of HR model previous findings in constrained flow, such a discrepancy can be reasonably attributed to an under sizing of k_s parameter assumed in the experimental model. Nonetheless, the systematic underestimation of pressure losses may also indicate flow separation within the outlet diffuser that cannot be captured through RANS simulations. Within this scenario, pressure losses associated with possible flow separation cannot be seized either by the proposed experimental approach or by the numerical model. Heated wall temperature predictions exhibited increasing deviation from experimental measurements at higher Reynolds numbers. However such an offset results acceptable when considering additional uncertainties arising from both experimental conditions and numerical modelling. During the high-temperature trial, no clear evidence of changes in effluent gas composition was detected. The speed-of-sound sensor recorded a slight increase that is more plausibly attributed to temperature variations in the bypass line rather than hydrogen formation. The comparison between the potentially coked and clean configurations yielded a possible evidence of heat transfer degradation. However, in light of methodological and experimental limitations, the Nusselt number approach proposed in this study does not guarantee a direct assessment of coke layer effects. With regards to the fluid heat pick-up, while the first test point showed an increased absorbed heat, the other exhibited variable reductions. In spite of these observations, it can't be concluded effectively that coking layer deposited on the heated base surface. Furthermore, the adopted methodology distributes any heat-flux variation uniformly along the channel, preventing clear identification of localized heat-transfer deterioration where coking might have occurred.

7 | Future developments

The outcomes of the present research activity highlighted several limitations related to both the adopted methodology and the MERiT experimental configuration, affecting methane heat transfer characterisation as well as thermal decomposition assessment.

Firstly, fluid-flow modelling through the channel may be significantly affected by possible flow separation in the outlet diffuser, whose influence on flow variables can be particularly difficult to capture. A redesign of this element to ensure a smoother flow transition would likely improve the reliability of reconstructed fluid variables. Moreover, the currently implemented experimental modelling does not account for extreme compressibility effects that may arise when very high pressure drops occur across the channel and connecting elements. Should future investigations involve rougher configurations leading to substantial pressure losses, the experimental reconstruction of fluid variables needs to be reformulated to seize more severe compressibility associated effects.

With regard to methane cracking investigation, thermal decomposition could not be reliably inferred through real-time sensors nor through comparison of the measured heat transfer coefficients. The uncertainty related to the time window selection for test points identification together with the intrinsic transient nature of conducted trials, in fact, may condition the Nusselt number comparison. Surely a sensitivity investigation addressing this window selection influence on the compared results may elucidate such an aspect. Furthermore, more direct approaches could be employed to detect the possible occurrence of coking layer depositions. For example, TWH readings response during thermal transients could be monitored and compared between coked and clean cases.

Given the uncertainty surrounding the occurrence of methane decomposition, post-test inspection of the channel inner surfaces is essential to verify whether carbon deposition has taken place. If no deposits are observed, it may be concluded that the channel temperatures reached during testing were insufficient to activate thermal decomposition process, being primarily limited by the maximum operating temperature of the electrical cartridges. In such a case, upgrading the heating system with cartridges capable of operating at higher temperatures would be essential to enable the MERiT facility to reach

methane cracking conditions, at least with Haynes230 samples.

Bibliography

[1] Richard Ristic. *A High Heat Flux Facility Design for Testing of Methane in Rocket Nozzle Cooling Channels*. 2017 (cit. on pp. 3, 37, 47, 71).

[2] Marcus Pettersson. *Cooling Potential of Methane in Rocket Nozzle Cooling Channels*. 2019 (cit. on pp. 3, 37, 47, 69).

[3] Jules C. Heldens et al. "On the characterization of methane in rocket nozzle cooling channels". In: *Acta Astronautica* 186 (Sept. 2021), pp. 337–346. ISSN: 00945765. DOI: 10.1016/j.actaastro.2021.05.034 (cit. on pp. 3, 4, 25, 37, 40, 44).

[4] Mohammadreza Kadivar et al. "A review on turbulent flow over rough surfaces: Fundamentals and theories". In: *International Journal of Thermofluids* 10 (May 2021), p. 100077. ISSN: 26662027. DOI: 10.1016/j.ijft.2021.100077 (cit. on pp. 7–16).

[5] Johann Nikuradse. "Nikuradse Laws of Flow in Rough Pipes 1933". In: *LAWS OF FLOW IN ROUGH PIPES* (1933) (cit. on p. 9).

[6] H. Schlichting. "Experimentelle Untersuchungen zum Rauhigkeitsproblem". In: *Ingenieur-Archiv* 7.1 (Feb. 1936), pp. 1–34. ISSN: 0020-1154, 1432-0681. DOI: 10.1007/BF02084166 (cit. on p. 9).

[7] C. F. Colebrook and C. M. White. *Experiments with fluid friction in roughened pipes* (cit. on p. 9).

[8] Curtis K. Stimpson et al. "Scaling Roughness Effects on Pressure Loss and Heat Transfer of Additively Manufactured Channels". In: *Journal of Turbomachinery* 139.2 (Feb. 1, 2017), p. 021003. ISSN: 0889-504X, 1528-8900. DOI: 10.1115/1.4034555 (cit. on pp. 9, 19, 35).

[9] Tuncer Cebeci. "General Behavior of Turbulent Boundary Layers". In: *Analysis of Turbulent Flows*. Elsevier, 2004, pp. 81–140. ISBN: 978-0-08-044350-8. DOI: 10.1016/B978-008044350-8/50004-X (cit. on pp. 10, 13).

[10] Albert A. Townsend. *The structure of turbulent shear flow*. 2. ed., transferred to digital printing. Cambridge monographs on mechanics and applied mathematics. Cambridge: Cambridge Univ. Pr, 1999. 429 pp. ISBN: 978-0-521-29819-3 978-0-521-20710-2 (cit. on pp. 11, 12).

[11] D.F. Dipprey and R.H. Sabersky. "HEAT AND MOMENTUM TRANSFER IN SMOOTH AND ROUGH TUBES". In: *International Journal Heat Mass Transfer* (1962), pp. 329–353 (cit. on pp. 12, 16–18).

[12] Karen A. Flack et al. "Experimental support for Townsend's Reynolds number similarity hypothesis on rough walls". In: *Physics of Fluids* 17.3 (Mar. 1, 2005), p. 035102. ISSN: 1070-6631, 1089-7666. DOI: 10.1063/1.1843135 (cit. on p. 12).

[13] Satish Kandlikar. *Heat Transfer and Fluid Flow in Minichannels and Microchannels*. Elsevier, 2006. 492 pp. ISBN: 978-0-08-044527-4 (cit. on p. 12).

[14] M R Raupach et al. *Rough-wall turbulent boundary layers* (cit. on p. 14).

[15] Jan Östlund. "Modelling of heat transfer in very rough cooling channels". In: (2024) (cit. on pp. 15, 18, 19, 48, 49, 68, 69).

[16] Karen A. Flack and Michael P. Schultz. "Roughness effects on wall-bounded turbulent flows". In: *Physics of Fluids* 26.10 (Oct. 1, 2014), p. 101305. ISSN: 1070-6631, 1089-7666. DOI: 10.1063/1.4896280 (cit. on p. 15).

[17] B. Aupoix and P.R. Spalart. "Extensions of the Spalart–Allmaras turbulence model to account for wall roughness". In: *International Journal of Heat and Fluid Flow* 24.4 (Aug. 2003), pp. 454–462. ISSN: 0142727X. DOI: 10.1016/S0142-727X(03)00043-2 (cit. on pp. 16, 70).

[18] B Aupoix. "Wall Roughness Modelling with k-w STT Model". In: () (cit. on p. 16).

[19] B. Aupoix. "Improved heat transfer predictions on rough surfaces". In: *International Journal of Heat and Fluid Flow* 56 (Dec. 2015), pp. 160–171. ISSN: 0142727X. DOI: 10.1016/j.ijheatfluidflow.2015.07.007 (cit. on pp. 16, 17).

[20] Beatrice Latini et al. "Modeling liquid rocket engine coolant flow and heat transfer in high roughness channels". In: *Aerospace Science and Technology* 126 (July 2022), p. 107672. ISSN: 12709638. DOI: 10.1016/j.ast.2022.107672 (cit. on pp. 17, 18).

[21] C.-J. Chen et al. "The Thermal Decomposition of Methane. I. Kinetics of the Primary Decompositionto C2 H6 + H2 ; Rate Constant for the Homogeneous Unimolecular Dissociation of Methane and its Pressure Dependence". In: *Canadian Journal of Chemistry* 53.23 (Dec. 1, 1975), pp. 3580–3590. ISSN: 0008-4042, 1480-3291. DOI: 10.1139/v75-516 (cit. on p. 19).

[22] Jules C. Heldens et al. "Assessment of sensors for the real-time detection of catalytic methane pyrolysis". In: *Fuel* 402 (Dec. 2025), p. 135860. ISSN: 00162361. DOI: 10.1016/j.fuel.2025.135860 (cit. on pp. 20, 21, 23).

[23] Kazuyuki Higashino et al. *Fundamental Study on Coking Characteristics of LNG Rocket Engines* (cit. on pp. 21, 22).

[24] Jules C. Heldens et al. “Effect of surface roughness on cooling channel fouling in methane fueled rocket engines”. In: *IAC-25.C4.2.3.x100049* (Oct. 2025) (cit. on pp. 23, 75).

[25] Shiyun Tang et al. “Relationship between Coking Behavior in Hydrocarbon Fuel Pyrolysis and Surface Roughness”. In: *Energy & Fuels* 32.2 (Feb. 15, 2018), pp. 1223–1229. ISSN: 0887-0624, 1520-5029. DOI: 10.1021/acs.energyfuels.7b03140 (cit. on p. 23).

[26] Lawrence L. Crynes and Billy L. Crynes. “Coke formation on polished and unpolished Incoloy 800 coupons during pyrolysis of light hydrocarbons”. In: *Industrial & Engineering Chemistry Research* 26.10 (Oct. 1987), pp. 2139–2144. ISSN: 0888-5885, 1520-5045. DOI: 10.1021/ie00070a034 (cit. on p. 23).

[27] C. Cockrell et al. “Transition in the supercritical state of matter: Review of experimental evidence”. In: *Physics Reports* 941 (Dec. 2021), pp. 1–27. ISSN: 03701573. DOI: 10.1016/j.physrep.2021.10.002 (cit. on p. 24).

[28] Raffaele Votta et al. “Experimental Investigation on Methane in Transcritical Conditions”. In: *50th AIAA/ASME/SAE/ASEE Joint Propulsion Conference*. American Institute of Aeronautics and Astronautics, July 28, 2014. ISBN: 978-1-62410-303-2. DOI: 10.2514/6.2014-4005 (cit. on pp. 24, 37, 38).

[29] Ibraheem Nasser et al. *INFLUENCES OF HYDROCARBON IMPURITIES ON HEAT TRANSFER DETERIORATION FOR SUPERCRITICAL LNG FLOWING IN COOLING CHANNEL* (cit. on p. 24).

[30] Bo Ruan and Hua Meng. “Supercritical Heat Transfer of Cryogenic-Propellant Methane in Rectangular Engine Cooling Channels”. In: *Journal of Thermophysics and Heat Transfer* 26.2 (Apr. 2012), pp. 313–321. ISSN: 0887-8722, 1533-6808. DOI: 10.2514/1.T3670 (cit. on p. 24).

[31] Hang Pu et al. “Numerical Method for Coupled Thermal Analysis of the Regenerative Cooling Structure”. In: *Journal of Thermophysics and Heat Transfer* 32.2 (Apr. 2018), pp. 326–336. ISSN: 0887-8722, 1533-6808. DOI: 10.2514/1.T5224 (cit. on p. 24).

[32] Xiao Hai et al. “Supercritical Heat Transfer of Methane in Regenerative Cooling Channels”. In: *Journal of Thermophysics and Heat Transfer* (July 22, 2025), pp. 1–14. ISSN: 0887-8722, 1533-6808. DOI: 10.2514/1.T7162 (cit. on p. 24).

[33] Raffaele Votta et al. “Experimental investigation of transcritical methane flow in rocket engine cooling channel”. In: *Applied Thermal Engineering* 101 (May 2016), pp. 61–70. ISSN: 13594311. DOI: 10.1016/j.applthermaleng.2015.12.019 (cit. on pp. 24–27, 37, 44).

[34] Jan Haemisch et al. "Experimental and Numerical Investigation of Heat Transfer Processes in Rocket Engine Cooling Channels Operated with Cryogenic Hydrogen and Methane at Supercritical Conditions". In: *TRANSACTIONS OF THE JAPAN SOCIETY FOR AERONAUTICAL AND SPACE SCIENCES, AEROSPACE TECHNOLOGY JAPAN* 19.1 (2021), pp. 96–105. ISSN: 1884-0485. DOI: 10.2322/tastj.19.96 (cit. on pp. 25–27).

[35] Billingsley et al. *Experimental and Numerical Investigations of RP-2 Under High Heat Fluxes* (cit. on pp. 26, 27, 38).

[36] Jens Fridh and Jan Östlund. *ON THE USE OF METHANE IN ROCKET NOZZLE COOLING CHANNELS* (cit. on p. 30).

[37] Inc. Haynes International. *HAYNES230 Alloy*. 2026. URL: https://haynesintl.com/en/alloys/alloy-portfolio/high-temperature-alloys/haynes-230/principal-features (cit. on p. 35).

[38] Aashna Raj et al. "Investigation of Pressure Drops in Additively Manufactured Haynes 230 Cooling Channels: Role of Surface Roughness". In: *76th International Astronautical Congress (IAC 2025)* (Oct. 29, 2025) (cit. on pp. 35, 41, 43–45, 48, 68, 69).

[39] Crane Co. *Flow of Fluids Through Valve, Fittings and Pipe*. 1999 (cit. on pp. 42, 43, 51, 53).

[40] A. Kayode Coker. "FLUID FLOW". In: *Ludwig's Applied Process Design for Chemical and Petrochemical Plants*. Elsevier, 2007, pp. 133–302. ISBN: 978-0-7506-7766-0. DOI: 10.1016/B978-075067766-0/50011-7 (cit. on p. 43).

[41] Ascher H. Shapiro. *The Dynamics and Thermodynamics of Compressible Fluid-Flow*. Vol. 1. The royal press company, 1953 (cit. on p. 44).

[42] ANSYS, Inc. *ANSYS CFX-Solver Theory Guide*. Canonsburg, PA, USA: ANSYS, Inc., 2020 (cit. on pp. 49, 70).

[43] P. R. Owen and W. R. Thomson. "Heat transfer across rough surfaces". In: *Journal of Fluid Mechanics* 15.3 (Mar. 1963), pp. 321–334. ISSN: 0022-1120, 1469-7645. DOI: 10.1017/S0022112063000288 (cit. on p. 53).

[44] B.S. Petukhov. "Heat Transfer and Friction in Turbulent Pipe Flow with Variable Physical Properties". In: *Advances in Heat Transfer*. Vol. 6. Elsevier, 1970, pp. 503–564. ISBN: 978-0-12-020006-1. DOI: 10.1016/S0065-2717(08)70153-9 (cit. on p. 54).

[45] Dawid Taler. "A new heat transfer correlation for transition and turbulent fluid flow in tubes". In: *International Journal of Thermal Sciences* 108 (Oct. 2016), pp. 108–122. ISSN: 12900729. DOI: 10.1016/j.ijthermalsci.2016.04.022 (cit. on p. 54).

[46] *Haynes 230 – Thermophysical Properties Database of Gen3 CSP Materials*. URL: https://gen3csp.gatech.edu/haynes-230/ (visited on 02/01/2026) (cit. on p. 88).

[47] R W Powell. *Thermal conductivity of selected materials*. 1966 (cit. on p. 88).

[48] U. Setzmann and W. Wagner. "A New Equation of State and Tables of Thermodynamic Properties for Methane Covering the Range from the Melting Line to 625 K at Pressures up to 1000 MPa". In: *Journal of Physical and Chemical Reference Data* 20.6 (Nov. 1, 1991), pp. 1061–1155. ISSN: 0047-2689, 1529-7845. DOI: 10.1063/1.555898 (cit. on p. 87).

[49] Sergio E. Quiñones-Cisneros and Ulrich K. Deiters. "Generalization of the Friction Theory for Viscosity Modeling". In: *The Journal of Physical Chemistry B* 110.25 (June 1, 2006), pp. 12820–12834. ISSN: 1520-6106, 1520-5207. DOI: 10.1021/jp0618577 (cit. on p. 87).

[50] Daniel G. Friend et al. "Thermophysical Properties of Methane". In: *Journal of Physical and Chemical Reference Data* 18.2 (Apr. 1, 1989), pp. 583–638. ISSN: 0047-2689, 1529-7845. DOI: 10.1063/1.555828 (cit. on p. 87).

[51] Luo Zhang et al. "Prediction and optimization of dimensional accuracy of inclined structures fabricated by laser powder bed fusion". In: *Journal of Manufacturing Processes* 81 (2022), pp. 281–289. DOI: 10.1016/j.jmapro.2022.06.078 (cit. on p. 88).

[52] *NIST TN 1297: Appendix A. Law of Propagation of Uncertainty*. Nov. 6, 2015 (cit. on p. 88).

A | Uncertainty analysis

The present work uncertainty analysis for experimental data processing consider both systematic and random uncertainties related to experimental set-up, variables sampling as well as fluid and material properties uncertainties. The main sources of uncertainties considered are listed hereafter:

- Instrumentation accuracy;
- Material and fluid properties uncertainties;
- Geometric uncertainty related to pieces manufacturing tolerances;
- Uncertainty related to probed parameters fluctuations over test points measurement period.

Instrumentation uncertainties have been related to their accuracy, based on their measuring range. Their percentage uncertainty is reported in Table A.1.

Quantity	**Instrument**	**Accuracy**	**% Uncertainty**
Pressure	Yokogawa EJX530A	±20 kPa	0.04
Differential pressure	Yokogawa EJX110A	±87 kPa	0.87
Temperature	Pentronic 810600	±1.5–±3.2 K	0.2–0.4
Mass flow	Yokogawa Rota-mass Nano	±0.00017 kg/s	0.5

Table A.1: Instrument uncertainties.

Material properties uncertainties considered have been retrieved through different references and listed in Table A.2.

Fluid properties uncertainties are extracted from literature reference which NIST CoolProp database builds upon [48–50]. Each physical property presents a degree of uncertainty related to certain areas of the element state diagram. Consequently, the employed uncertainties refers to typical fluid conditions experienced by methane during operations.

Concerning geometrical uncertainties, typical manufacturing tolerances of test section

Quantity	Reference	Material	% Uncertainty
Thermal conductivity	[46]	Haynes230	5.82 - 6.60
Thermal conductivity	Powell [47]	Copper	5
Thermal conductivity	Powell [47]	Au65Cu25 solder	7

Table A.2: Material properties uncertainties.

components have been assumed. Laser bed fusion process accuracy has been estimated through available works in literature, since the test article realisation was commissioned to an external provider. Zhang et al. [51], for example, investigated process accuracy variability for 60° inclined test pieces ranged between 20-100 μm for those directions parallel to the printing bed. Such values are reasonably dependent on the metal powder grain size as well as laser spot dimension that, unfortunately, were unavailable to the author. Nonetheless, test pieces surface roughness can provide a qualitative indication of average particle size. Considering that R_a for the present test article ranges between 11 μm and 19 μm, it is reasonable to assume that powder grain size utilised is not exceeding such a dimension. Average grain size for manufactured test pieces in the research by Zhang et al. [51] was approximately 34 μm. Consequently, manufacturing tolerances for the present test article cross section dimension were roughly assumed half of the highest observed deviation from nominal dimension by Zhang et al. [51] and equal to 50 μm. It has to be remarked that such an estimation has been based on not comparable printing directions of the test pieces, consequently tolerances values assumed in this work are only representative of the manufacturing process.

The uncertainty related to measured parameters variation over this probing periods for test point identification, is calculated by multiplying the standard deviation for each measurement point by the critical value of the Student's t distribution which is associated to the number of collected sample. All variational uncertainties, as well as all other uncertainty considered in this work refers to 95% confidence level.

Uncertainty propagation followed the one reported by NIST TN 1297 [52]. The combined standard uncertainty of a measurement result $u_c(y)$ and taken to represent the estimated standard deviation of the result y, can be expressed as illustrated in Eq. (A.1), assuming that parameters associated uncertainty are not cross-related.

$$u_c^2(y) = \sum_{i=1}^{N} \left(\frac{\partial f}{\partial x_i} \right)^2 u^2(x_i) \tag{A.1}$$

where f is the the function correlating y with the independent variables x_i. Following this definition, function derivatives have been retrieved analytically or numerically. For uncertainty propagation through CoolProp database for which analytical derivative formulation is unfeasible a numerical derivation has been carried out considering central differencing scheme, where the reference step size has been selected as $\max(\sqrt{\epsilon}, \sqrt{\epsilon} \cdot x_i)$, where ϵ is the machine epsilon. When referring to parameter yielded by implicit relation, applying such a propagation through derivative formulation results hardly applicable. Consequently, uncertainty propagation has not been carried out through these formulae.

List of Figures

List of Tables

List of Symbols

Variable	Description	SI unit
A	cross-sectional area	m^2
A^*	critical flow area	m^2
c_p	specific heat at constant pressure	$\mathrm{J\,kg^{-1}\,K^{-1}}$
D_h	hydraulic diameter	m
f	Darcy friction factor	–
C_F	Fanning friction factor	–
g_{2PP}	roughness regime transition function	–
HTC	convective heat transfer coefficient	$\mathrm{W\,m^{-2}\,K^{-1}}$
k	thermal conductivity	$\mathrm{W\,m^{-1}\,K^{-1}}$
k_s	equivalent sand–grain roughness height	m
k_s^+	roughness Reynolds number	–
k_f	roughness heat–transfer parameter	–
K	resistance coefficient	–
L_{entr}	hydrodynamic entrance length	m
M	Mach number	–
$\dot{m}$	mass flow rate	$\mathrm{kg\,s^{-1}}$
Nu	Nusselt number	–
p	static pressure	Pa
p_0	total pressure	Pa
Pr	Prandtl number	–
Pr_t	turbulent Prandtl number	–
q''	heat flux	$\mathrm{W\,m^{-2}}$
Q	heat transfer rate	W
R	specific gas constant	$\mathrm{J\,kg^{-1}\,K^{-1}}$
Re	Reynolds number	–
S_a	arithmetic mean surface height	m
S_q	root mean square surface height	m

Table A.3 continued

Variable	Description	SI unit
S_{sk}	surface skewness	–
S_{ku}	surface kurtosis	–
St	Stanton number	–
T	static temperature	K
T_0	total temperature	K
T_b	bulk fluid temperature	K
T_s	wall surface temperature	K
U^*	friction velocity	$\mathrm{m\,s^{-1}}$
u	flow velocity	$\mathrm{m\,s^{-1}}$
x	streamwise coordinate	m
y^+	dimensionless wall distance	–
δ	boundary layer thickness	m
ρ	fluid density	$\mathrm{kg\,m^{-3}}$
ν	kinematic viscosity	$\mathrm{m^2\,s^{-1}}$
γ	specific heat ratio	–
Δp	pressure drop	Pa
ΔU^+	roughness function velocity shift	–

Acknowledgements

Finally we arrived, maybe, to the most important section of this document. The author apologises for any missing formalism, but he preferred to full throttle his emotions and gratitude at the end of this academic journey that hopefully represented just the beginning of whatever is coming next.

DISCLAIMER: due to the many nationalities of people mentioned hereafter, this section will encompass a weird mixture of languages.

First of all, huge thanks to Jens, Jules, Aashna, Taras, Jan, Matts and Leif, who drove the presented work to his best potential and, before that, gave to this unknown italian guy the possibility to be formed in a completely thriving and stimulating environment which EGI department undoubtedly represented for him. I will never forget all those teachings coming from your experienced guidance and, above all, your kindness and patience in letting me learn from my own mistakes. Definitely, you provided to me something more than just a thesis research opportunity but expertises and mindsets that sooner or later will turn to be extremely useful both in my personal and professional life. Tack så mycket.

Special thanks to prof. Paravan who enlighten this work through his invaluable suggestions and experienced support, and, before that, provided the author the opportunity to have this unforgettable thesis research experience in a foreign country, together with offering his supervision from more than 1000 km distance.